2020

Very high cycle fatigue behavior of laser beam-powder bed fused Inconel 718 considering the layer orientation and surface finish effects

Palmer Frye
University of North Florida, n00889866@unf.edu

University of North Florida

School of Engineering

Master's Thesis

Summer 2020

Very high cycle fatigue behavior of laser beam-powder bed fused Inconel 718 considering the layer orientation and surface finish effects

by Palmer R. Frye

Committee members:

Dr. Jutima Simsiriwong, *Advisor*

Dr. Paul Eason

Dr. Alexandra Schonning

Palmer Frye
Redacted

Approved by the thesis committee: **Date**

_____ _____

Dr. Jutima Simsiriwong

Committee Chairperson

_____ _____

Dr. Paul Eason, Committee Member

_____ _____

Dr. Alexandra Schonning, Committee Member

Dedication

This work is wholeheartedly dedicated to my beloved parents and dearest Emily, whose unwavering love, support, and encouragement have inspired me to never quit in the pursuit of my goals, no matter the circumstances.

Acknowledgments

I am forever indebted to my graduate advisor, Dr. Jutima Simsiriwong, for her unending support, relentless encouragement, and most of all for her patience. I do not know if I could ever pay you back for the experience you have helped me gain. I hope that this thesis report provides you with some sort of satisfaction. Also, I wish you continued success with your future graduate students.

I am very fortunate to have received guidance from my other two thesis committee members, Dr. Paul Eason, and Dr. Alexandra Schonning. Thank you for research assistance and words of wisdom. Each of you have been a tremendous support throughout my graduate research journey. Additionally, my sincere gratitude goes to Dr. Paul Eason for helping me gather data throughout the lockdown.

I would also like to acknowledge my MSERF co-workers and friends, Dr. Albina Mikhaylova, Dr. Brian Wingender, and Justin White. Each of you was subjected to countless hours of listening to my research success stories and frustrations. Thank you for your constant support.

Thank you to my colleagues from the Auburn University's National Center of Additive Manufacturing Excellence, Dr. Nima Shamsaei, Dr. Shuai Shao, and Muztahid Muhammad. I hope that we can remain research colleagues for life.

Lastly, I would like to acknowledge the National Aeronautics and Space Administration (NASA), through the University of Central Florida's NASA Florida Space Grant Consortium, for helping to fund this research.

Contents

List of Figures

List of Tables

Abbreviations

AM	Additive manufacturing
BSE	Back-scatter electron
CAD	Computer aided design
D	Diagonal/diagonally
DED	Direct Energy Deposition
EBSD	Electron back-scatter diffraction
EDS	Energy dispersive spectroscopy
FCC	Face centered cubic
HCF	High cycle fatigue
HV	Vickers hardness
HIP	Hot isostatic pressing
LB-PBF	Laser beam-powder bed fusion
LoF	Lack of fusion
S-N	Stress-life
SE	Secondary electron
SEM	Scanning electron microscope
USF	Ultrasonic frequency
VHCF	Very high cycle fatigue
V	Vertical/Vertically

Symbols

R	Stress ratio
σ_{min}	Minimum stress
σ_{max}	Maximum stress
σ_a	Stress amplitude
σ_w	Fatigue limit
$2N_f$	Reversals to failure

Abstract

Additive Manufacturing (AM) techniques have recently gained popularity for fabrication of parts used in aerospace applications. Some of these parts may be subjected to cyclic loading at very high frequencies, leading to service life requirements exceeding ten-million cycles (>10^7 cycles). Therefore, understanding the very high-cycle fatigue (VHCF) behavior of these AM parts is an important step in their design and qualification processes. In this thesis, both high-cycle fatigue (HCF) and VHCF behaviors of Inconel 718, a Ni-base superalloy, manufactured via a Laser Beam-Powder Bed Fusion (LB-PBF) process, are investigated. Uniaxial, fully reversed force-controlled fatigue tests were conducted utilizing a ultrasonic fatigue test system operating at 20 kHz. Specimen fracture surfaces were analyzed using a scanning electron microscope (SEM). Fatigue test specimens were fabricated in two different build orientations, including vertical and 45 degrees (i.e., diagonal) with respect to the build plate, and subjected to a post-process solution annealing and aging heat treatment. In addition, specimens were testing in both the as-built and post-process machined condition. Fatigue response of LB-PBF Inconel 718 was compared to that of wrought Inconel 718.

Comparison of the stress-life (S-N) response of LB-PBF Inconel 718 fabricated in the vertical and diagonal build orientations showed almost no discrepancy in fatigue life for the as-built condition. For machined LB-PBF specimens, the effects of build layer orientation were more apparent: fatigue resistance of vertically oriented specimens was superior to diagonally oriented specimens. An increase in fatigue resistance of LB-PBF Inconel 718 was observed for specimens of the machined surface condition due to the removal of surface defects from the as-built surface. AM process induced defects significantly influenced fatigue crack initiation for as-built specimens: all fatigue cracks in as-built specimens originated from either surface micro-notches

or sub-surface lack of fusion. Fatigue cracks in all specimens, regardless of build orientation and surface quality, were found to initiate from both specimen surfaces and sub-surface anomalies in the microstructure. Fatigue limit estimation was performed using Murakami's approach, which accounts for AM process induced defects. Additionally, S-N curve fitting was performed using the Basquin equation. Despite the presence of defects seen on VHCF fractures of as-built vertical specimens, the Murakami model proved to be insufficient for the specimens used in this study.

1. Introduction

In aerospace engines, combustion temperatures can exceed 1,000 ˚C, which means that the material of choice for critical engine components must withstand high temperatures without sacrificing mechanical performance. Aircraft engine components such as turbine and compressor blades require a long service life before an overhaul is required. Typically, airline engines are required to be refurbished or replaced after 15,000 hours of use. Additionally, these components are subjected to cyclic loading at very high frequency, which results in service lives that commonly exceed ten-million cycles ($>10^7$ cycles). Nickel-based superalloys are a common material choice for jet engine components such as turbine and compressor blades due to their high resistance to corrosion and oxidation as well as excellent mechanical properties at high operating temperatures.

Metal additive manufacturing (AM) techniques, such as laser beam-powder bed fusion (LB-PBF), have recently been of great interest to the aerospace industry for its significant potential to replace conventional manufacturing methods as a production method for jet engine components. Since no special tooling or molds are required to build a part via AM, LB-PBF is expected to allow for more complex part geometries and less material waste when compared to machining. Although the popularity of AM of metals has increased tremendously, the structural integrity of parts produced via LB-PBF is not fully understood. AM using metal powders and their resulting microstructure and property relationships have not been adequately characterized for use in critical aerospace engine applications. For AM to replace conventional manufacturing methods as a means of production, the mechanical response of LB-PBF parts under cyclic loading must be fully understood.

2. Review of the literature

2.1. Additive manufacturing of metallic materials

Metallic powder-based AM methods can form high density metallic parts in a layer-wise fashion [1-3]. LB-PBF is a class of AM technologies that is oriented to manufacturing functionally graded parts [2]. A schematic of the LB-PBF process is shown in Figure 1. The build platform is presented with a thin layer of powdered material. A laser, or overhead heat source, is used to selectively melt the material at distinct locations throughout the powder bed. When a layer is completed, the build platform indexes down-ward and a fresh layer of powdered material is deposited on top of the previously built layer.

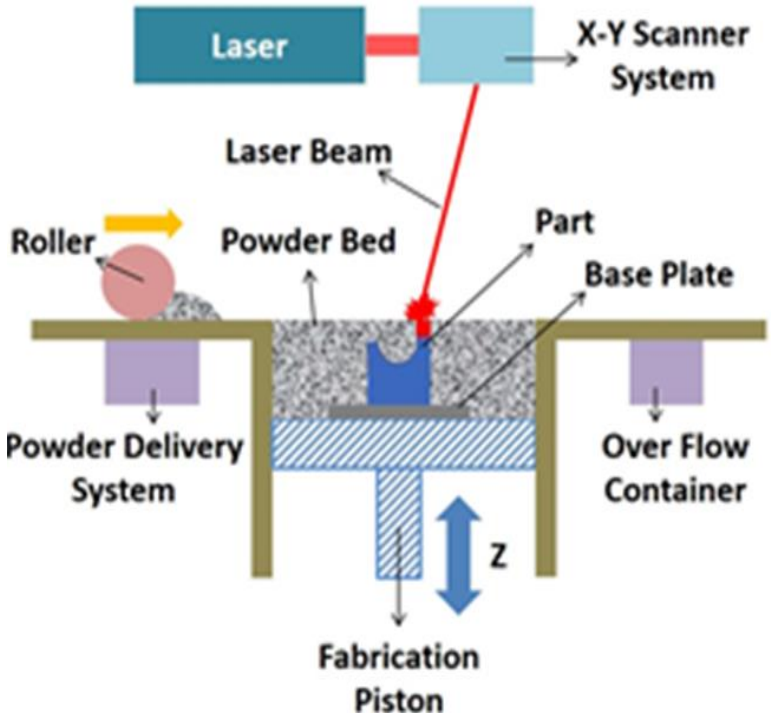

Figure 1. Schematic of the LB-PBF process [3].

Metal AM processes like LB-PBF have unique qualities and advantages over conventional processes such as casting, forging, and computerized numerical control (CNC) machining [1]. For AM processes, it is additive or bottom up; therefore, no special tooling or fixtures are required [1-3]. LB-PBF technologies only require a computer aided design (CAD) model of a part and the metal powder that is to be used. Parts and assemblies with complex geometries can be produced in a single step, and the part geometry is no longer dictated by the manufacturing process. This has the potential to save material waste, machine downtime, and other manufacturing costs [1].

A major limitation of AM metals is the lack of material characterization and mechanical behavior research, which prevents use of 3-D printed metallic parts for structural applications [4]. Additionally, the process parameters for which metal powder-based AM technologies operate are not yet standardized, which can result in inconsistent part production quality [3, 5]. AM process parameters must be optimized such that detrimental process induced microstructural defects are reduced to provide adequate tensile strength that is comparable (or superior) to wrought material counterparts [2].

Metallic parts that are produced using LB-PBF contain numerous defects that are inherent to the process [6, 7]. These defects include lack of fusion (LoF) of melted or partially melted metal powder between build layers, entrapped gas pores, voids, and poor as-built surface finishes [6, 8]. These defects are not optimal for structural components, as they act as stress concentration points that can accelerate catastrophic fracture if they are not properly accounted for [6, 8, 9]. Most of these defects can be attributed to non-ideal process parameters and build conditions, such as incorrect laser energy, laser scan speed, humidity of the build chamber, and metal particle size distribution [8]. It is important that the effects of each defect type on mechanical properties are fully understood.

One of the most often occurring process induced defects is LoF. These defects form during the build process when metallic powder particles are not fully melted and bonded to previously deposit metal layers [6, 8]. These defects can form on both part surfaces and sub-surfaces between build layers. LoF defects are usually a result of insufficient overlap of successive melt pools between layers [8].

In LB-PBF technologies, parts are fabricated in a vacuum chamber that is purged with Ar gas [1, 2]. The rapid heating of metal powder leads to the entrapment of Ar gas within the melt pool. Insufficient melt-pool cooling time restricts the proper outgas of Ar before solidification [9]. This results in entrapped gas pores within parts. In some cases, empty spaces between metal powder particles are not filled during melting and solidification of build layers, which leads to the presence of larger pores, referred to as micro-voids since they are measured on a micro-meter scale [9]. Presence of micro-voids and entrapped gas pores reduces the relative density of parts and can cause both local and bulk reductions in strength of the material [10].

Lastly, AM parts may experience noticeable flaws on part surfaces, such as artificial notches, stair-stepping, and separation between build layers [11-13]. These types of surface flaws act as stress concentrations, which can be detrimental to mechanical properties [8, 14]. Surface defects are characteristic of parts built in a powder bed, as un-melted powder particles bond the part surfaces while the laser-melted metal solidifies. Post process machining and polishing of part surfaces is the most common method to minimize the detrimental effects of surface defects on a part's mechanical performance [1, 3, 4].

It is considered to be challenging to fully understand the effects of the as-built surface on the mechanical behavior of AM metallic parts. As-built AM specimens are not usually built to the same dimensional tolerances of test specimens that have been machined. In many cases, AM parts

contain surfaces or features that are impossible to access via a CNC machine or polishing media. As-built specimens are expected to experience failure on part surfaces; however, they are still capable of experiencing failure due to a large number of pores and internal defects [15].

2.1.1. Wrought and additively manufactured Inconel 718

Functionally graded AM metals, such as nickel-based superalloys, are of great interest to the aerospace industry for their noteworthy combination of exceptional mechanical properties including high tensile strength, corrosion resistance, and creep rupture resistance in applications with a wide range of operating temperatures [16-19]. Inconel 718 is a particular nickel-based superalloy grade that is commonly used in gas-power turbines, jet engines, and rocket engine components, as it is able to maintain adequate mechanical properties at temperatures up to 650 ˚C [15-18]. The processing-microstructure-mechanical property relationships for Inconel 718 have been widely researched for specific applications, such as high temperature rocket engine components and jet engine turbine or compressor blades [17, 20-22].

The microstructure of wrought Inconel 718 is heavily dependent on the forming process [23]. Wrought Inconel 718 is typically forged into plate or round bar stock; however, it can also be used for investment casting. Inconel 718 is a precipitation hardened alloy; therefore, its microstructure is heavily influenced by post-forming heat treatment [17, 21, 23, 24]. The typical chemistry of the alloy Inconel 718 is presented in Table 1. The material matrix is comprised of FCC γ phase (space group Fm-3m) containing nickel and chromium [21-23]. Depending on the chemistry and processes used in production of the alloy, the presence of intermediate phases can significantly influence the material's mechanical properties [21-23].

Table 1. Acceptable chemical composition ranges of Inconel 718 [21, 23].

Element	Wt. %	Element	Wt. %	Element	Wt. %
Al	0.2 - 0.8	Cu	Max 0.3	Ni	50 - 55
B	Max 0.006	Fe	17	P	Max 0.015
C	Max 0.08	Mn	Max 0.35	S	Max 0.015
Co	Max 1	Mo	2.8 - 3.3	Si	Max 0.35
Cr	17 - 21	Nb	4.75 - 5.5	Ti	0.65 - 1.15

Figure 2 below displays the space groups, Wyckoff positions, and lattice parameter information established from characterization of wrought Inconel 718. Inconel 718 contains many secondary phases in the form of γ' and γ'' and minor (trace amounts of) secondary phases such as metal carbides, δ precipitates, and Laves phase. The γ' phase (space group Pm-3m) is given a chemical formula of Ni_3(Ti, Al, Nb) as its composition varies depending on the weight percentages of the micro-constituents Ti, Al, and Nb [20]. The γ' phase is responsible for Inconel 718's high strength at elevated temperature [20]. The body centered tetragonal γ'' phase (space group I4/mmm) can contribute to increased hardness of the alloy; however, this phase is only semi-coherent with the matrix [20, 22]. γ'' precipitates can undergo a slow transformation to a needle like δ precipitates (space group Pmmn) with an orthorhombic unit cell [20, 22]. Some improvement of strength can be attributed to trace amounts of δ precipitates; however, many have reported to increased cracking sensitivity at elevated temperatures resulting from a high volume-fraction of δ precipitation [16, 24, 25].

Phase	Space Group	Lattice parameter range[2]	Wyckoff positions					
			Element	Notation	X	Y	Z	Sof*
NbC[7]	225 - Fm-3m	a = 0.430–0.470	Nb	4a	0	0	0	0.192
			C	4b	0.5	0.5	0.5	0.230
Matrix[8]	225 - Fm-3m	a = 3.591	Cr	4a	0	0	0	0.5
			Ni	4a	0	0	0	0.5
$\delta-Ni_3Nb$[9]	59 - Pmmn	a = 0.3624–0.511 b = 0.421–0.4251 c = 0.452–0.4556	Nb	2a	0	0	0.667	1
			Ni	2b	0	0	0.5	1
			Ni	4f	0.25	0	0.167	1
$\gamma''-Ni_3Nb$[10]	139- I4/mmm	a = 0.3624 c = 0.7406	Nb	2a	0	0	0	1
			Ni	2b	0	0	0.5	1
			Ni	4d	0	0.5	0.25	1
γ'[11]	221 - Pm-3m	a = b = c = 0.3561–0.3568	Al	1a	0	0	0	1
			Ni	3c	0.5	0.5	0	1
TiC[12]	225 - Fm-3m	a = 0.430–0.470	Ti	4a	0	0	0	0.26
			C	4b	0.5	0.5	0.5	0.44

Figure 2. Inconel 718 phases including space groups, Wyckoff positions, and lattice parameters [21].

Inconel 718 mechanical properties are heavily determined by the location and amount of precipitates within the matrix [21, 24]. Solution annealing and aging is a heat treatment method used to control the amount of these precipitates. The AMS 5662 standard is a designation for Inconel 718 forgings. This standard specifies that the stock material was first held at a minimum of 10 minutes (per inch of thickness of the stock material) at a solution set temperature of 954°C. It is subsequently transferred to a separate furnace and held at 718°C furnace for 8 hours, and 621°C for a total precipitation time of 18 hours [26]. The expected microstructure of Inconel 718 after following this heat treatment standard is shown in Figure 3 below.

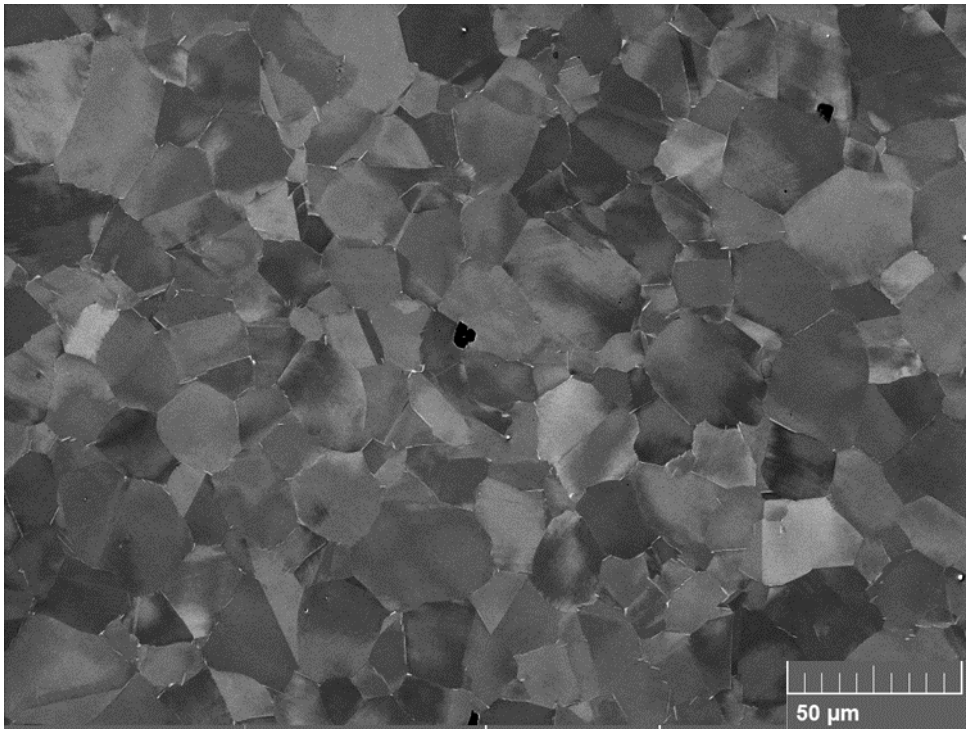

Figure 3. AMS 5662 wrought Inconel 718 microstructure showing equiaxed γ grains.

Inconel 718 that is solution annealed and aged to the AMS 5662 standard will contain an equiaxed grain structure with intergranular precipitation. The micrograph in Figure 4 shows the morphology of these intergranular precipitates: they appear as both intergranular needle and plate-like δ phase (with white appearance under scanning electron microscopy, SEM). Trace amounts of metal carbides (typically titanium carbides and niobium carbides) and nitrides can also be found throughout the metal matrix. Varying solution heat treatment parameters are known to affect the location and presence of the incoherent δ phase precipitates [21]. Furthermore, the manner in which the metal is processed can yield microstructures that are unlike what is shown in Figure 3 and Figure 4.

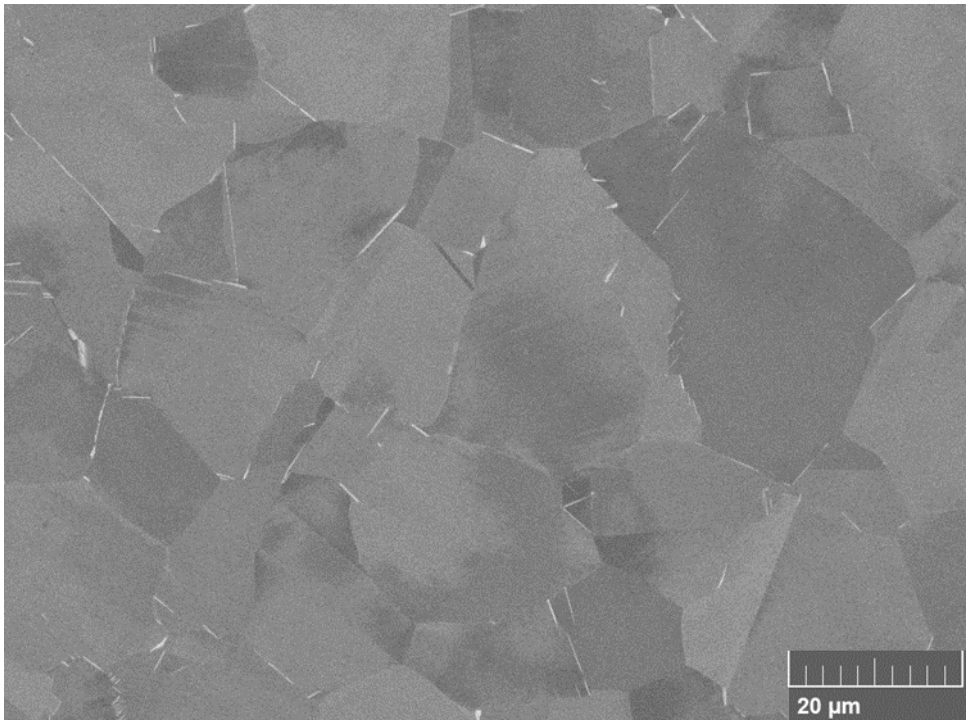

Figure 4. Micrograph of wrought Inconel 718 showing a closeup of the equiaxed γ grains with intergranular precipitation of δ phase.

Metal powder-based AM methods are known to yield microstructures that are not similar to their commercially available counterparts [1, 3]. During the LB-PBF fabrication process, each layer of material experiences extremely rapid solidification, as well as some degree of heating and cooling as each successive layer is deposited overhead. The high energy laser has a short interaction time with a small area of metal powder, resulting in high thermal gradients across the build layer. Following rapid solidification and shrinkage of the metal, high residual thermal stresses are induced resulting in an unstable material [1]. The LB-PBF build process yields an Inconel 718 microstructure with highly directional dependent grain growth, formation of non-equilibrium phases (such as Laves and MC's), and micro-segregation of elements like Nb and Mo [17, 20, 22, 25]. Figure 5 depicts an electron back-scatter diffraction (EBSD) map of as-built

Inconel 718. The representative microstructure in Figure 5 shows the directional dependence of the grains with respect to the programmed build direction.

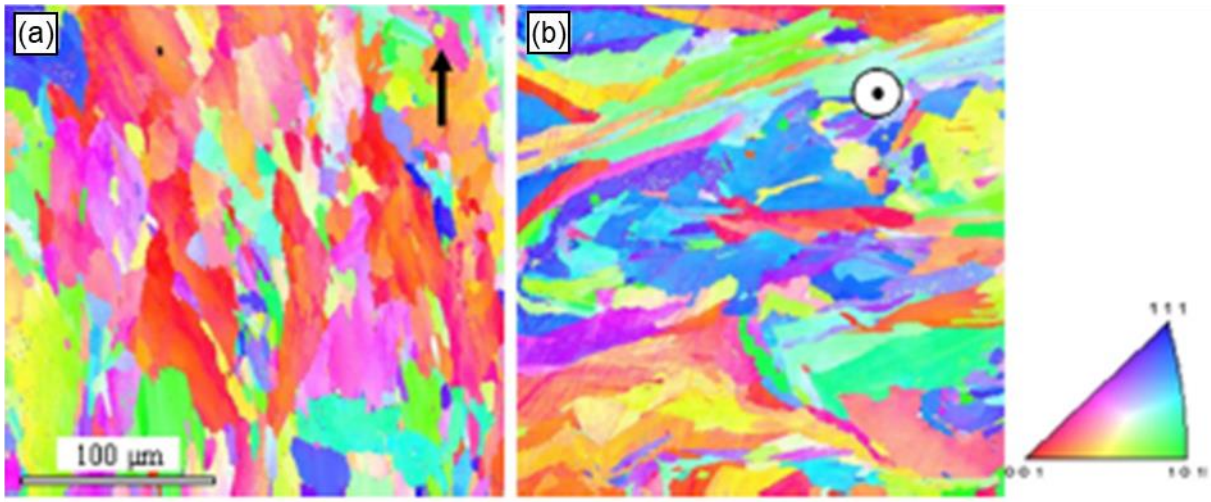

Figure 5. EBSD maps of as built AM Inconel 718 showing (a) columnar grain grow parallel to the build direction (black arrow) and (b) normal to a build layer [22].

2.2. Very high cycle fatigue behavior of metals

Mechanical components such as turbine or compressor blades in aerospace engines are subjected to cyclic loading, meaning the applied load on a component fluctuates with respect to time. The mechanism for which failure of mechanical components subjected to cyclic loading is referred to as fatigue. Fatigue failure accounts for up to 90% of all mechanical failures, therefore extensive material testing and modeling are a necessary benchmark for engineers to properly design parts to withstand cyclic loading [26].

The stress-life (S-N) curve of Figure 6 is obtained by subjecting a representative metal test specimen to a cyclic stress at a predetermined stress amplitude [27]. The test terminates when fatigue failure is achieved. The number of cycles experienced by each test before fatigue failure

occurs is referred to as fatigue life. Figure 6 shows the general trend: as applied cyclic stress amplitude decreases, the fatigue life increases. The traditional S-N curve is typically limited to 10^7 cycles. Fatigue failures that occur in the regions between point A and point B on the S-N plot of Figure 6 are referred to as High Cycle Fatigue (HCF) failures. For materials such as steels, the slope of the S-N curve approaches a horizontal asymptote at around 10^6 cycles [26, 27]. The point at which the slope of the curve becomes horizontal is referred to as the "knee point" (point B) after which the material will no longer experience fatigue failure, even up to 10^7 cycles. The stress that corresponds to the knee point is referred to as fatigue limit. Components subjected to cyclic loading beyond 10^7 cycles are said to experience "infinite life."

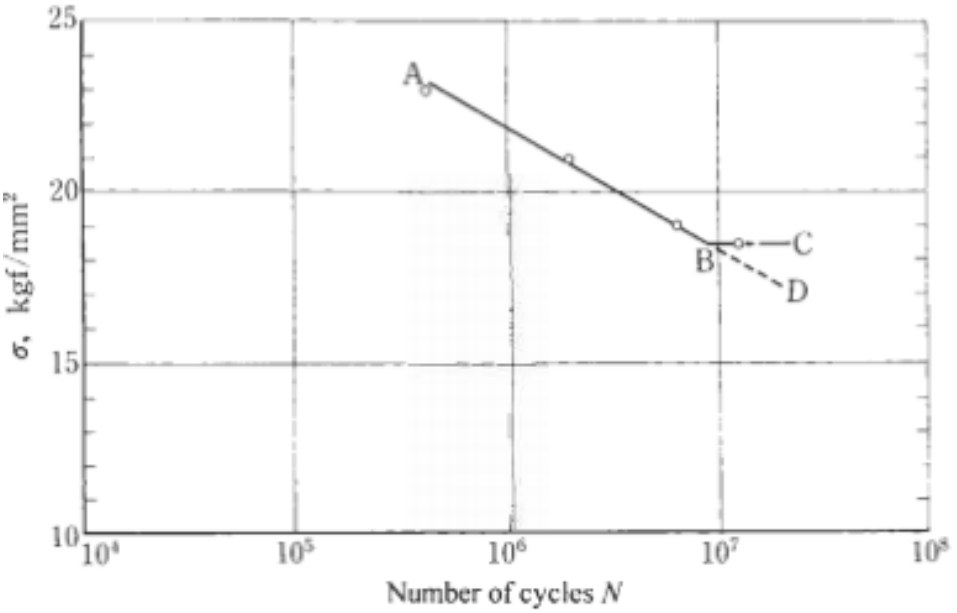

Figure 6. S-N Curve of steel showing knee point [27].

Depending on the loading frequency and service life, a part, such as a jet turbine compressor blade, is required to resist fatigue failure well beyond 10^7 cycles [27, 28]. The fatigue regime that corresponds to fatigue lives exceeding 10^7 cycles is referred to as the Very High Cycle Fatigue (VHCF) regime. Various researchers [18, 29-35] have performed S-N studies utilizing

high frequency fatigue testing methods and have successfully proved that fatigue failure can occur past 10^7 cycles, even for materials with a supposed fatigue limit.

Metal fatigue is a progressive, irreversible process that consists of three stages: fatigue crack initiation, propagation, and overload fracture [26]. In the VHCF regime, fatigue crack propagation only accounts for a small portion of fatigue life. Rather, it is said that up to 90% of the total fatigue life is spent in the fatigue crack initiation stage for a part that fails in the VHCF regime [36]. On the contrary, fatigue failures that occur in the Low Cycle Fatigue (LCF) regime initiate cracks much sooner, and the majority of fatigue life is spent propagating fatigue cracks [26, 36]. Short service life parts, i.e. parts that are may fail in the LCF regime, can be routinely examined for the presence of fatigue cracks. Fatigue cracks in long service life parts, such as jet turbine and compressor blades, cannot be detected because they do not form until soon before catastrophic failure. Therefore, a sound understanding of the various factors that influence VHCF behavior is crucial for the designer.

High frequency and conventional axial VHCF behavior investigations of wrought Inconel 718 have reported that fatigue cracks are capable of initiating at sub-surface anomalies and weak points in the microstructure. The main sources of sub-surface crack initiation as reported by Texier et al. [34] are metal carbides, TiN clusters, and large γ grains randomly dispersed throughout the matrix. Crack initiation from carbides happens in early stages of fatigue due to the brittle nature of carbides. For this reason, a large presence of carbides within the microstructure of Inconel 718 parts can significantly reduce fatigue strength. Cracks initiating in large austenite grains can be identified by the presence of persistent slip bands between grain boundaries [34]. As suggested by [34], The two main sources of sub-surface crack initiation are brittle metal carbides and coarse grains containing twin boundaries with elastic incompatibility induced stress concentrations

greater than high angle grain boundaries. It is proposed that there exists an optimal value for austenite grain size as well as the population of carbides within the matrix to achieve the highest VHCF resistance for wrought Inconel 718 [34].

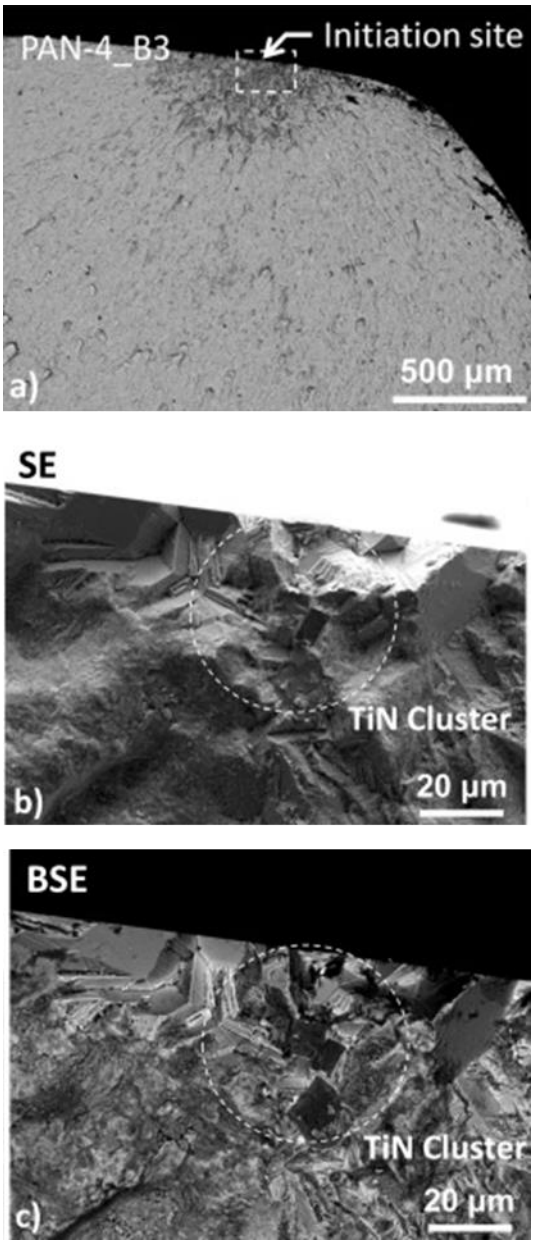

Figure 7. Fatigue crack originating at TiN cluster. This specimen was tested at Δε=0.44% with a corresponding fatigue life of 5.7×10^6 cycles. The overall fracture is shown in (a) and the magnified crack initiation site is shown in (b) & (c) [34].

Assessment of the structural integrity of additively manufactured components subjected to cyclic loading requires knowledge of the many factors that influence fatigue failure or crack initiation. In most cases there is insufficient information to produce a trustworthy mathematical model to predict fatigue life, especially in the VHCF regime. Fatigue research has expanded, however, to investigate the effects of critical flaws induced from laser-based AM processes such as LB-PBF and Direct Energy Deposition (DED). Many pre-existing fatigue life prediction models have been successfully applied to various metal parts produced via AM, however in the case of LB-PBF Inconel 718, there is still a lack of information on this subject [5].

For AM Inconel 718, there is only one published study regarding its VHCF behavior. Yang et al. [31] performed high frequency fatigue tests on IN718 specimens produced using a LB-PBF process. In their study, the AM fatigue specimens contained a variety of process-induced defects, consistent with the ones in [9, 27, 30, 32, 33, 35], such as entrapped gas porosity, LoF defects, and directional grain growth (i.e., columnar grains normal to the build platform). Fatigue cracks were shown to have originated from multiple sources concurrently, such as a grain that is near to a large pore, especially in the higher range of the HCF regime (i.e, 5 x 10^6 cycles). Uncertainty of failure mode presents a challenge for parts that are required to last longer than 10^7 cycles. The results published by Yang et al. [31] showed that LB-PBF IN718 specimens tested at the same stress amplitude as wrought specimens have much lower fatigue resistance resulting in shorter fatigue lives An overall reduction in internal defects such as LoF between build layers is a possible means for increasing the LB-PBF material's VHCF resistance as compared to the wrought counterparts [31].

Additional AM metals such as titanium alloy, aluminum alloy, and steels have been of great interest for the aerospace industry, especially for applications that require resistance to cyclic

loading [5, 28]. Other researchers have shown that fatigue performance of AM metals is greatly influenced by the process induced defects, similar to the results published by Yang et al. [31]. Gunther et al. [35] studied the fatigue behavior of LB-PBF Ti-6Al-4V subjected to high frequency cyclic loading via a high frequency fatigue tester. In the HCF regime, AM Ti-6Al-4V experiences fatigue failure from surface and sub-surface fatigue cracks [35]. In the HCF regime, the AM process induced defects that are most likely to initiate fatigue cracks are LoF voids. At higher stress amplitudes, fatigue failure is most likely to occur as a result of LoF defects that are in touch with the surface or just below the surface of a test specimen. An example of a surface fatigue failure site can be seen in Figure 8. It appears that the fatigue crack initiated due to a large LoF defect in touch with the specimen surface.

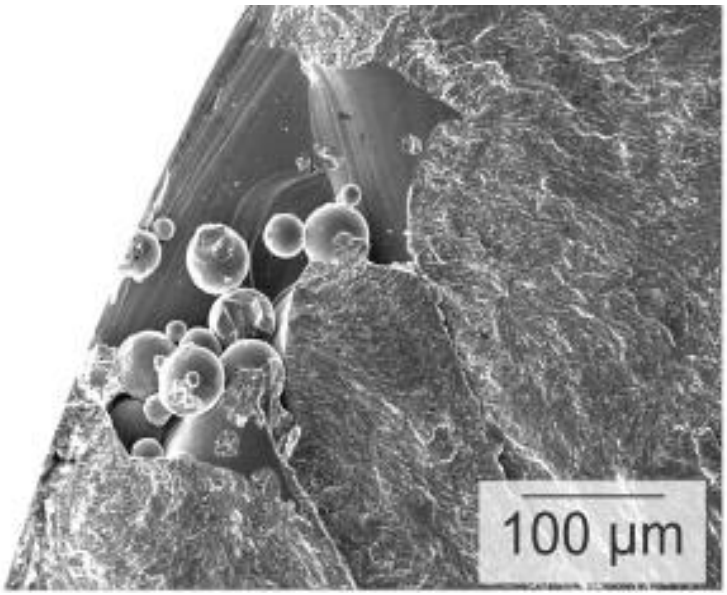

Figure 8. Surface failure initiation site at LoF defect in LB-PBF Ti-6Al-4V sample with a fatigue life of $N_f = 1.56 \times 10^5$ cycles [35].

As fatigue life exceeds 10^7 cycles, AM Ti-6Al-4V experiences an apparent shift in fatigue failure mechanism from surface to the sub-surface [35]. LoF defects like in Figure 8 are not limited

to specimen surfaces, they can also exist the center of the specimen, such as that in Figure 9. These defects lack uniformity in shape and size and are dispersed randomly throughout the microstructure. The fracture surface in Figure 9 is that of a specimen which failed as a result of a large, sub-surface LoF defect.

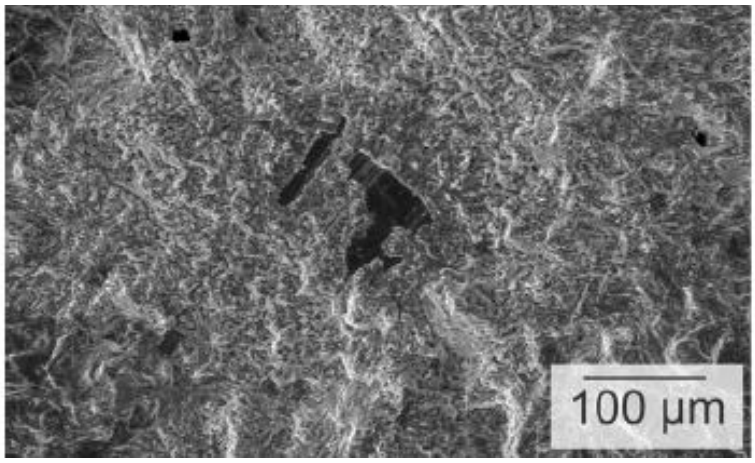

Figure 9. Internal LoF defect fracture surface in LB-PBF Ti-6Al-4V sample with a fatigue life of at $N_f = 1.17 \times 10^7$ cycles [35].

Entrapped gas pores and micro-voids in test samples seemed to have the most significant influence on fatigue resistance [35, 37]. Gunther et al. [35] compared two batches of test specimens built under the same process parameters; however, one batch of test specimens was post process Hot Isostatic Pressed (HIPed) and the other batch was only stress relieved. Figure 10 compares the S-N performance of these two batches. The HIP process significantly reduced the porosity of the specimens and as a result drastically improved VHCF performance as compared to the non-HIPed batch [35]. However, even the HIPed specimens still contain some remnant porosity and voids, which shows that the HIP process only minimizes the presence of entrapped gasses. Micro-voids cannot be removed by any post processing techniques; therefore, process parameter optimization is the only means of reducing micro-void presence [37].

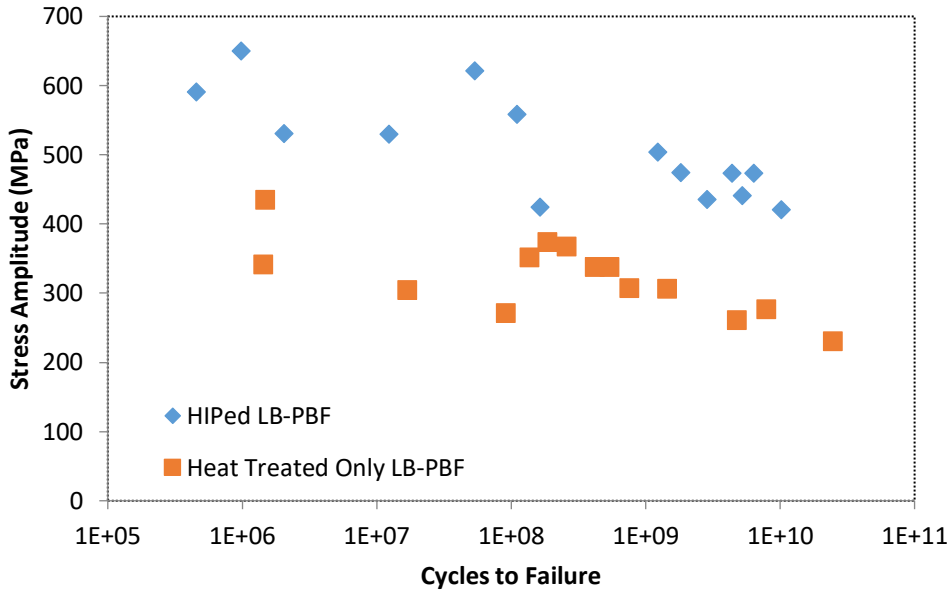

Figure 10. Comparative S-N curves of two LB-PBF Ti-6Al-4V test specimen batches showing significant improvement of fatigue resistance after post-process HIP [35].

2.2.1. Effects of surface roughness and layer orientation

The LB-PBF process builds parts layer-by-layer, which tends to produce sharp stair-step notches on part surfaces due to 3-d contouring in parts. LB-PBF part surfaces contain un-melted metallic powder particles, since solidification of melted metal occurs in a powder bed. Part surface quality tends to exhibit a directional dependence, in which planes or faces that are normal to the z direction of the build platform have the best surface quality, while surfaces that are parallel or angled to the z direction tend to have the worst surface quality.

Poor surface texture is a critical flaw of as-built AM metallic parts [38]. In addition, the topography is complex and difficult to characterize in detail due to the peak heights, spacing, and feature qualities on part surfaces [11, 12]. A correlation between poor surface quality of AM metallic parts and their behavior under cyclic loading has not been fully realized. Gunther et al.

[38] investigated the effects of surface roughness on HCF behavior of AM Ti-6Al-4V through internal channels built into the fatigue specimens, as shown in Figure 11.

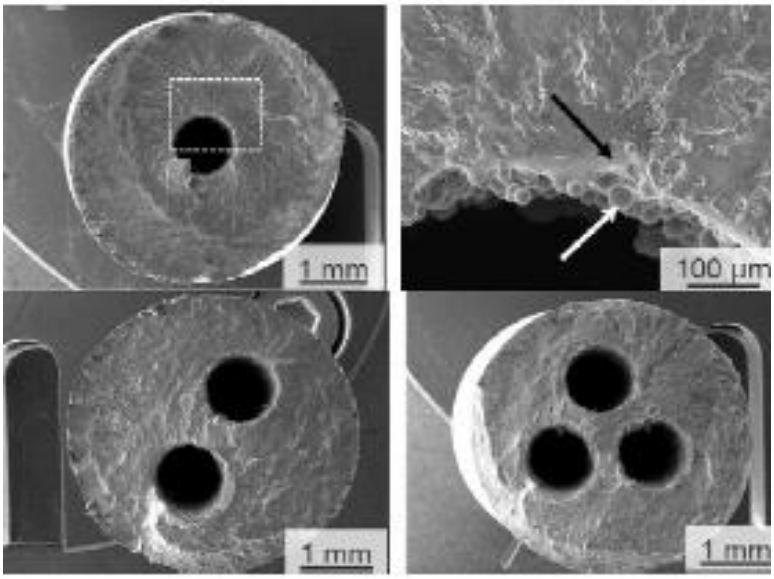

Figure 11. Internal channels in AM fatigue specimens [38].

In HCF regime failures, fatigue cracks are expected to initiate from the specimen surface, especially if the specimen surface contains flaws from processing or machining. In the case of the as-built surface of LB-PBF parts, the presence of unfused powder particles, LoF in touch with the surfaces, and separation between build layers are likely crack initiation sites. Gunther et al. [38] reported a strong presence of unfused particle clusters at crack initiation sites, as seen in Figure 11. A close-up of this site is shown in Figure 12. Although this study reported a strong dependence on surface roughness for crack initiation, Gunther et al. [38] did report multiple crack initiation sites at sub-surface locations due to the presence of remnant porosity and LoF defects. It has been mentioned that fatigue failure in the VHCF regime uniquely originates from sub-surface defects, but with the lack of knowledge of surface roughness effects on VHCF behavior, it is still an

important consideration that should be further studied. The results by Gunther et al. [38] suggest that the need for a fatigue limit at 10^9 cycles is critical for enhancing fatigue performance and service life of AM metallic parts.

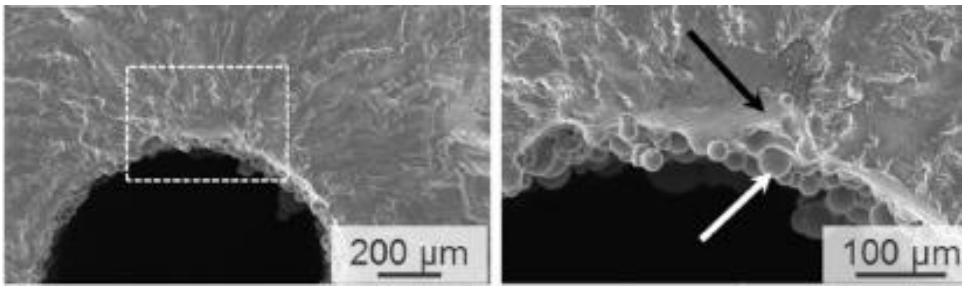

Figure 12. Fatigue failure in AM Ti-6Al-4V specimen resulting from surface flaws [38].

One of the challenges associated with AM is predicting how a part's mechanical behavior will be affected by its build layer orientation [1, 4]. AM is a bottom-up manufacturing process, which means that parts are fabricated by adding layers of material to pre-existing layers until the end geometry is achieved [1]. Compared to machined parts, AM metallic parts exhibit a correlation between build direction and mechanical properties. Some studies have noted that surface quality can be optimized or even degraded depending on the build layer orientation as well as by varying AM processing parameters [11-13, 39]. Parts built at an incline tend to exhibit a directional dependence of surface roughness, where high amounts of un-melted powder particles form heavy clusters on the *down-skin* and *up-skin* sides of parts as shown in Figure 13.

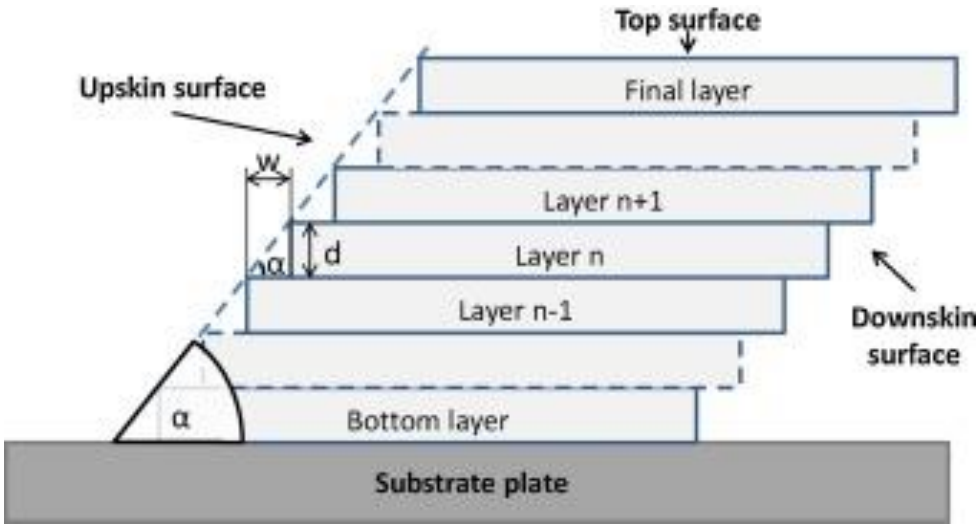

Figure 13. Schematic showing the up-skin and down-skin sides of an AM part that is inclined with respect to the build direction [40].

Although build layer orientation has been shown to affect surface quality, studies of the effects of build layer orientation on fatigue performance of AM metallic have not proven any direct correlations. Fatigue behavior does not depend on build layer orientation, rather the orientation and size of the internal defects such as LoF and porosity [32, 41-43]. Figure 14 shows the three build orientations of 0, 45, and 90 degrees with respect to the build platform. These three build directions are the most commonly tested orientations.

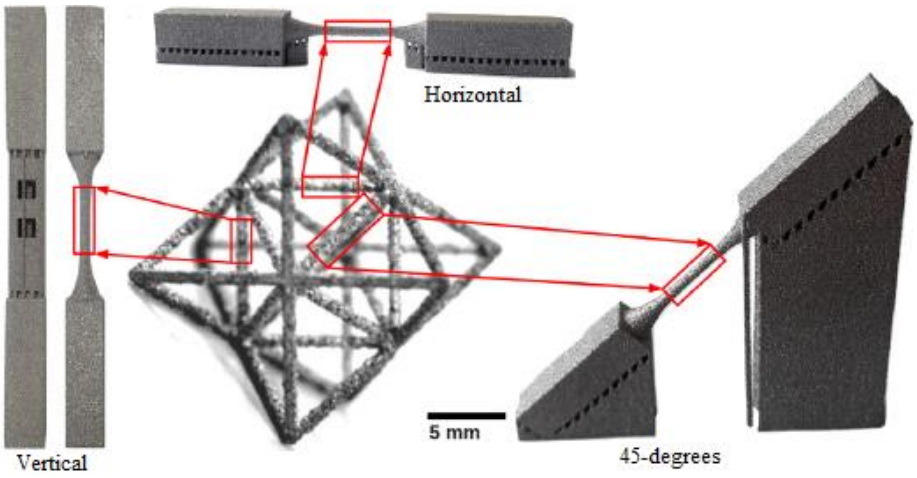

Figure 14. Build orientation variety of AM metallic parts [39]

It can be best concluded that the relationship between build layer orientation and fatigue behavior depends on the orientation of surface defects and density of internal defects, which directly correlates to the build direction [33, 39]. No conclusions can be made for the VHCF regime, as there is still a lack of studies on build direction effects. It may be speculated that the orientation of sharp notches on part surfaces will have little effect on VHCF performance of AM metallic parts, since VHCF cracks originate predominantly at sub-surface defects [18, 30-33, 35]. However, the correlation between build layer orientation and defect density may have significant effect on VHCF performance, which is an important consideration.

2.2.2. Very high cycle fatigue test methods

Fatigue testing up to 10^7 cycles is usually achieved with servo-hydraulic or rotating bending testing machines, which typically operate at a loading frequency between 20 and 50 Hz for most metals. At a test frequency of 50 Hz, one fatigue test of a metallic specimen up to 10^7 cycles is achieved in just over 55.5 hours. VHCF testing (after 10^7 cycles) is a very costly and time-consuming task for conventional fatigue testing machines. At the same 50 Hz frequency, a single test up to 10^9 cycles will take 5,555 hours or 231.5 days. To aid in the reduction of time and cost

associated with long life fatigue testing, the operating technique known as USF testing was introduced [44]. Testing times can be significantly reduced thanks to the USF operating frequency of 20 kHz. Specimens operating at this frequency must be axially symmetrical, contain a reduced cross section to amplify the vibration, and have the appropriate length such that longitudinal waves and maximum stresses are at the center of the reduced diameter gauge section. The geometry of the USF specimen type is shown in Figure 15 below.

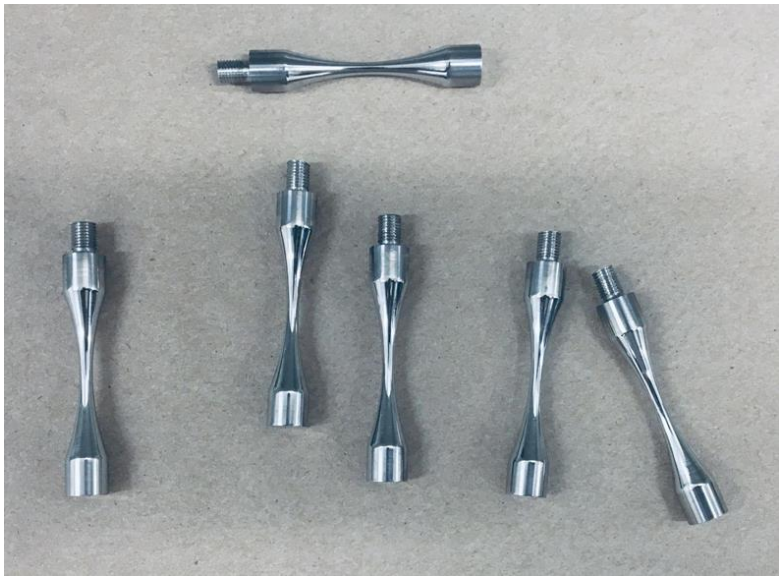

Figure 15. USF hourglass specimens

There are no current ASTM testing standards for USF testing; therefore, each material's test specimen geometry must be calibrated by the researcher [44]. During testing, the test specimen temperature must be closely monitored, as specimen self-heating is a likely result of the high frequency vibrations. Since displacement of the specimen is measured by a high-resolution extensometer, it is imperative that specimen temperatures remain constant, as specimen thermal expansion will yield erroneous extensometer readings [44]. Temperature rise is typically

minimized using coolant (air or liquid) flow directly to the gauge section of the test specimen, as well as intermittent driving pulse/pause conditions to negate thermal expansion effects from self-heating. Intermittent pulse/pause parameters typically vary between 110 and 4000 milli-seconds depending on the stress amplitude. Tests are terminated when the observed change in resonance frequency of the test sample exceeds 500 Hz. Figure 16 shows an overview of the Shimadzu USF-2000A, an ultrasonic fatigue test machine at the University of North Florida Department of Mechanical Engineering. The Shimadzu USF-2000A provides displacement controlled, fully reversed (R = -1) loading at a frequency of 20 kHz at room temperature.

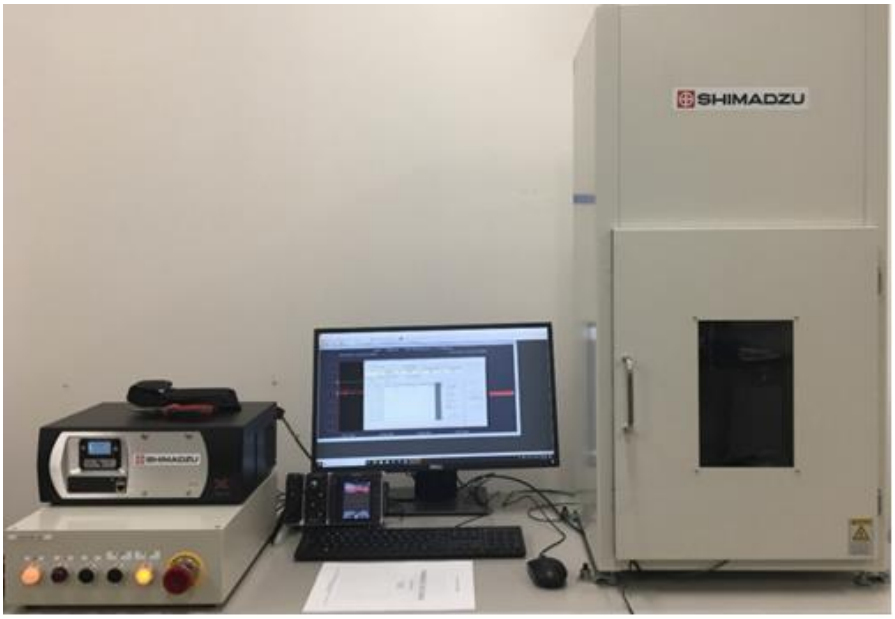

Figure 16. Image of the Shimadzu USF-2000A test setup at the University of North Florida's School of Engineering.

2.3. Fatigue life modelling

2.3.1. S-N curve approximation

The purpose of S-N fatigue research is to produce usable data for design of mechanical components that are subjected to cyclic loading. S-N data for materials under specific loading

conditions such as variable stress amplitude and loading frequency is often limited or unavailable, therefore approximations through S-N models must be made. One of the most commonly used S-N curve fitting techniques was introduced by Basquin [26], which utilizes a power-law function for straight line log-log S-N curves, which gives the following equation:

$$\sigma_{N_f} = A(N_f)^b \quad (1)$$

where σ_{N_f} is the R = -1 fatigue strength at N_f cycles. The coefficient A and the exponent b are material specific values and must be determined experimentally. The value A can be selected as the material ultimate tensile strength, or as an intercept that fits the linear regression. The value b represents the slope of the S-N curve, and typically is found to be in the range of -0.05 to -0.2 [26]. The Basquin model is often used to approximate fatigue life for materials that show a constant slope throughout the entire S-N curve. The accuracy of the Basquin equation is decreased for materials that exhibit S-N slope variation that is depended of the fatigue life regime [26].

2.3.2. Defect-sensitive fatigue life modelling using Murakami's approach

In fatigue life prediction, a practical point of interest is estimating the fatigue limit of a material at 10^9 cycles. Fatigue models that account for influence of non-metal inclusions throughout the metal matrix are difficult to obtain mainly because size, location, and shape of inclusions cannot be predicted reliably. The American Society for Testing and Materials (ASTM) proposed a rating system for inclusions in various engineering materials. Inclusions are surveyed based on chemistry and geometry [27].

It has been determined by Murakami [27] that the two basic quantities of the material's Vickers hardness (H_v) and the effective area of the failure initiating defect are the basis for fatigue life estimation of components containing microstructural defects. The material parameter H_v has

been shown to correlate to fatigue strength of many engineering materials [27]. Typically, materials with higher Vickers hardness values demonstrate higher fatigue strength, however if a specimen contains a notch or artificial defect, this correlation diminishes. This phenomenon is due to the occurrence of non-propagating cracks. The threshold stress intensity factor (ΔK_{th}) is not directly proportional to Vickers hardness with the presence of micro-notches. Instead, it follows the function:

$$\Delta \mathrm{Kth}\ \alpha\ (\mathrm{Hv}\ +\ \mathrm{C}) \tag{2}$$

where C is dependent on the material of interest.

Instead of the parameter of interest being threshold stress intensity factor, the fatigue limit σ_w or threshold stress value in which a component experiences infinite fatigue life, is substituted for this analysis. Murakami [27] proposed the relationship between fatigue limit, defect projected area, and Vickers hardness as:

$$\sigma_w\ =\ \frac{1.43(Hv\ +\ 120)}{(\sqrt{area})^{\frac{1}{6}}} \tag{3}$$

Application of Eq. (3) has produced reliable results, in which actual fatigue life data was within an error of 10% for aluminum alloys, steels, titanium, and nickel alloys. Austenitic stainless steels ventured outside of the 10% error margin due to testing instability from martensitic transformation [27]. The general form of Murakami's model for fatigue limit prediction follows the general form:

$$\sigma_w\ =\ \frac{C(Hv\ +\ 120)}{(\sqrt{area})^{\frac{1}{6}}} \tag{4}$$

In which the constant 1.43 is replaced by C, a constant that varies based on the location of the fatigue failure initiating defect with respect to the test specimen's outer surface. In the case of

additively manufactured metallic test specimens, numerous intrinsic defects are randomly scattered throughout the bulk material. Often, LoF voids, and pores can exist on specimen surfaces, in contact with the specimen surface, or below the specimen surface. Each of these cases, depicted in Figure 17, is appropriated a value for the constant C in Eq. (5).

C = 1.43 for the case of surface defects
C = 1.41 for the case of defects in contact with the specimen surface (5)
C = 1.56 for the case of defects below the specimen surface

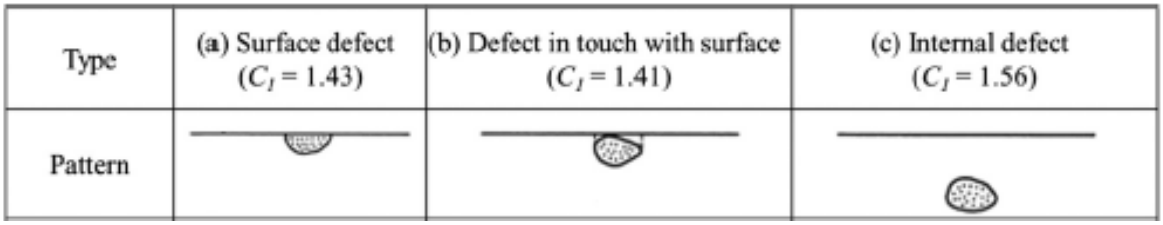

Figure 17. Classification of defects according to their location [27, 35].

3. Experimental procedure

3.1. Material and specimen fabrication

Test specimens were fabricated using an LB-PBF process via the EOS M290 additive manufacturing system in an argon purged environment. Suggested process parameters provided by the manufacturer for the EOS M290 system (see Table 2) were utilized for all AM part fabrications in this study. All LB-PBF specimens were fabricated at the National Center of Additive Manufacturing Excellence, Auburn University

Table 2. Suggested EOS M290 build process parameters used in fabrication of Inconel 718 fatigue test specimens.

Laser power	285 W
Scanning speed	960 mm/s
Hatching space	110 μm
Layer thickness	40 μm
Shielding gas type	Argon

Parts were fabricated using two build directions, vertical (V) and diagonally (i.e., 45 degrees with respect to the build plate, D) using the oversized and net shape dimensions and geometries shown in Figures 18(a) and 1(b) for USF fatigue tests. The net shape dimensions in Figure 18(b) represents the desired specimen geometry. After fabrication, all specimens were subjected to heat treatment according to AMS5662 for nickel alloy parts. Following this procedure, specimens were first held at a minimum of 10 minutes at a solution set temperature of 954°C. They were subsequently transferred to a separate furnace and held at 718°C furnace for 8 hours, and

621°C for a total precipitation time of 18 hours. After heat treatment, the oversized specimens were then machined using a computer numerical control (CNC) lathe to the final dimensions shown in Figures 18(b). Specimens tested in the as-built surface condition (hereafter referred to as "as-built" specimens) were fabricated according to the net shape dimensions in Figure 18(b). The dimensions and geometries of the USF specimens in Figure 18(b) were established based on the recommendation by the USF fatigue test system manufacturer, Shimadzu Scientific, to achieve the required natural frequency.

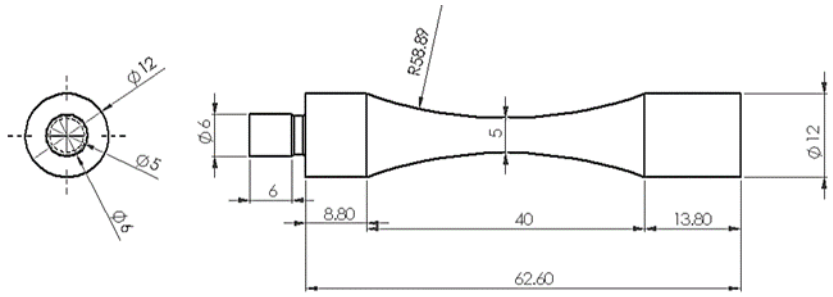

(a)

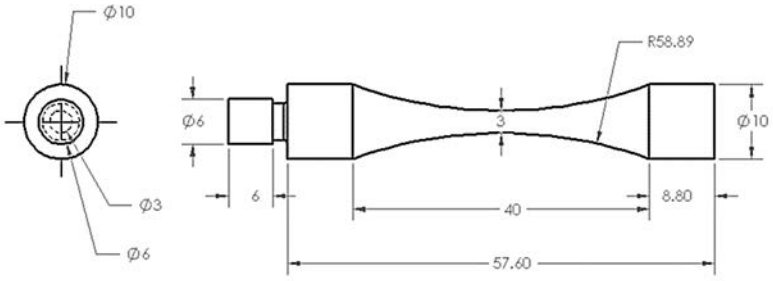

(b)

Figure 18. Dimensions and geometries of USF fatigue specimens used in this study. The drawing in (a) is for oversized specimens that were post-process machined for enhanced surface quality. The drawing in (b) represents the net shape specimen dimensions.

Additionally, wrought specimens for USF testing were fabricated from 15.9 mm round bar stocks and machined using a CNC lathe. As-received wrought Inconel 718 bars were processed

and heat-treated to achieve the AMS 5662 standard; therefore, no additional heat treatments were applied to wrought Inconel 718 specimens. Following machining, all specimens, including wrought and post-process machined LB-PBF ones, were polished using 400 grit, 800 grit, 1000 grit, 1500 grit, and 2000 grit silicon carbide cloths, respectively, to remove machining marks from their surfaces. Lastly, SEM images were post-process analyzed via ImageJ software. This technique was used to achieve area measurements for crack initiating defects. Fatigue limit calculations were performed using Microsoft Excel.

3.2. Microstructural and fractographic analyses

Initial microstructural analysis and fractographic analysis was performed using a Tescan Mira3 field emission SEM operating at an accelerating voltage of 15 kV. SEM fractography analysis was performed using the secondary electron (SE) imaging mode. SEM micrographs were obtained using the back-scatter electron (BSE) mode to show phase and chemistry contrast in images. Metallography samples were prepared by sectioning fatigue specimens along the planes that lie transverse and radial to the loading direction, as shown in Figure 19. Wrought and LB-PBF Inconel 718 representative microstructural images including grain characteristics were investigated by EBSD measurements using an Oxford system. Specimen chemical composition and phase identification was performed using energy dispersive spectroscopy (EDS) analysis under SEM.

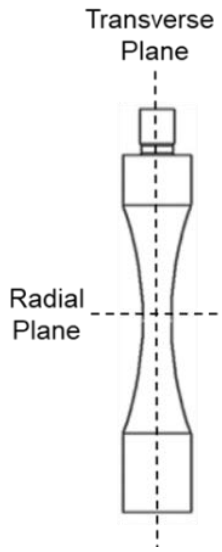

Figure 19. Lines showing transverse and radial planes of fatigue specimens for microscopy sample preparation.

Metallographic samples were sectioned using a slow speed saw and experienced preliminary grinding and polishing with 120 grit, 240 grit, 400 grit, 600 grit, 1200 grit grinding discs, and 6μm and 1μm lapping films with polishing pads, respectively. To ensure the consistent surface quality in all specimens, a final vibratory polishing was performed using a 0.02 μm lapping film for 12 hours. Surface quality analysis was conducted using a Keyence VHX-6000 digital microscope in 3-D depth and composition mode. 3D image stacking at the gauge section of each specimen revealed the unique surface features of LB-PBF specimens fabricated in differing build directions. The average roughness, R_a, was obtained for one representative test specimen of both as-built V and as-built D build conditions. A profile length of 1.5 mm was used for measurement on four locations of the gauge section of each specimen. Higher-resolution fracture surface imaging was performed using the Tescan Mira3 field emission SEM operating at 1-5 kV to identify crack nucleation, fatigue striations, and crack propagation regions.

3.3. Fatigue testing

Fatigue testing in this study was conducted under R = -1 loading at 20 kHz at room temperature and relative humidity, employing a Shimadzu USF-2000A ultrasonic fatigue test system. Figure 20 shows the functional principle of the USF fatigue test system setup. A piezo actuator oscillates at a frequency of 20 kHz, which sends stationary longitudinal waves through the amplify horn and test specimen, thus allowing the test specimen to resonate. The dimensions and geometry of the specimen are designed so that the maximum stress is applied to the gauge section only, and the maximum displacement occurs at the free end and the clamped end of the specimen.

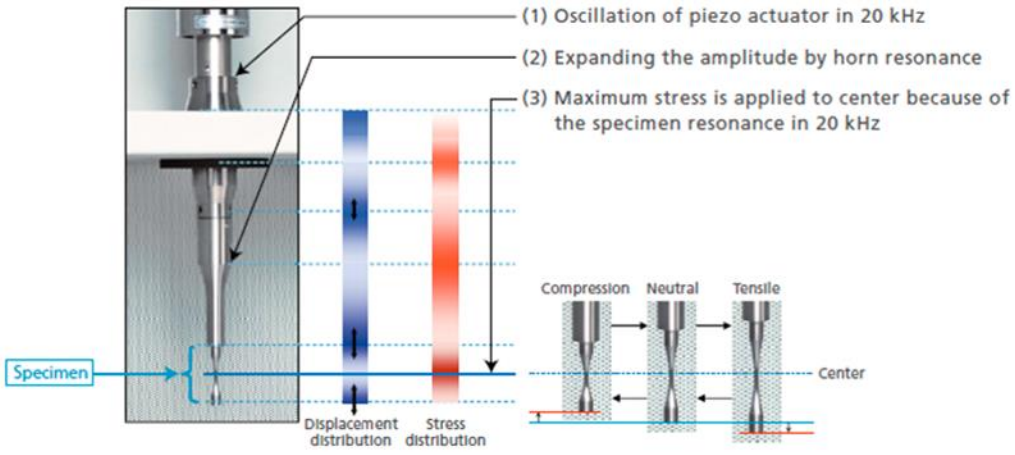

Figure 20. Functional principle of the Shimadzu USF-2000A fatigue test system [44].

During testing, the specimen temperature was closely monitored using a laser thermometer. The temperature rise of the specimen was kept less than 30 °C to minimize any temperature effects on the results. Temperature rise was also minimized using compressed coolant (air) flow directly to the gauge section of the specimen, as well as intermittent driving pulse/pause conditions to negate thermal expansion effects from self-heating. Intermittent pulse/pause parameters varied

from 110/800 msec to 110/4000 msec, depending on the stress amplitude. Calibrations of extensometer and piezo-electric transducer were carried out prior to testing. Each test is terminated when the observed change in the resonance frequency of the test sample exceeds 500 Hz. The run-out for USF fatigue testing was set to $2x10^9$ reversals.

4. Experimental results

4.1. Microstructural characterization

The overall chemistry of wrought Inconel 718 specimens was provided through certification of the supplier, Online Metal Supply, and is shown in Table 3. The material matrix is the face centered cubic (FCC) γ phase containing primarily Ni and Cr, with alloying elements Fe, Nb, Ti, C, & Mo. The alloy also contains intermediate phases throughout the matrix in the form of γ' and γ'' as well as trace amounts of titanium carbides. The γ' phase is the secondary strengthening phase, with a chemical formula of (Ni, Co)3(Al, Ti), and has an ordered L12 cubic lattice structure coherent with the matrix.

Table 3. Overall chemistry provided by material supplier certification for wrought the wrought Inconel 718 used in this study

Element	Weight %
Ni	53.1
Nb	5.2
Cr	20.2
Mo	3.1
Ti	0.8
Al	0.3
Fe	REM

The main strengthening phase of Inconel 718 is the ordered body centered tetragonal (D022 structure) γ" phase, with a chemical formula of Ni3Nb, that is semi-coherent with the matrix. However, the γ" phase can transform to the brittle, orthorhombic δ phase if operating temperatures exceed 650°C leading to significant reduction in strengths therefore limits the service temperature ceiling of the alloy. δ phase precipitation is mostly intergranular, therefore, intergranular cracking from high amounts of δ precipitates is a typical failure mode in high-temperature applications of Inconel 718. Figure 21 displays the microstructure of wrought Inconel 718, as obtained through BSE imaging.

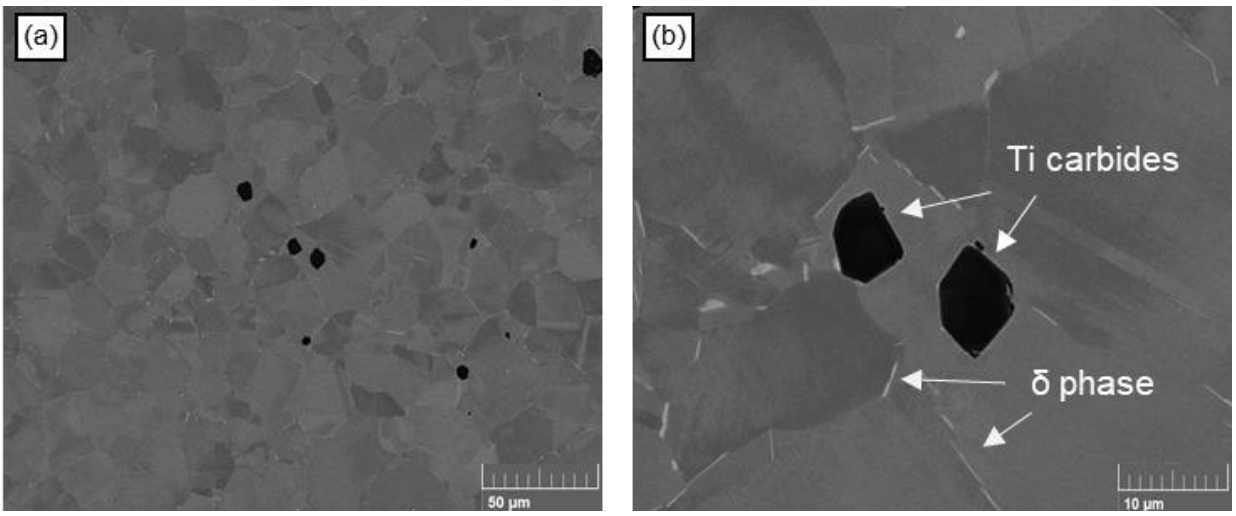

Figure 21. Transverse BSE micrographs of wrought Inconel 718. The overall image in (a) is magnified in (b) to show the presence of titanium carbides and intergranular δ precipitates.

Conventionally-processed as well as AM Inconel 718 can also contain trace amounts of an additional secondary phase known as Laves phase (chemical formula (Ni,Fe,Cr)2(Nb,Mo,Ti)); however, based on the morphology of the precipitates observed in the micrographs shown in Figure 4, it was best concluded that both the wrought material used in this study were considered to be free of Laves phase. Two main types of precipitates observed in the wrought microstructure were

intergranular δ phase and carbides containing titanium, shown in Figure 21(b). These phases were identified by comparing their chemistries (obtained through EDS line-scan of the precipitates) and morphologies to the same precipitates observed in the literature [21, 23].The grain structure of the matrix is considered to be equiaxed, therefore the microstructure of the transverse plane matched the microstructure of the radial plane. A representative microstructural image was obtained via EBSD analysis for wrought Inconel 718 and the results are presented in Figure 22.

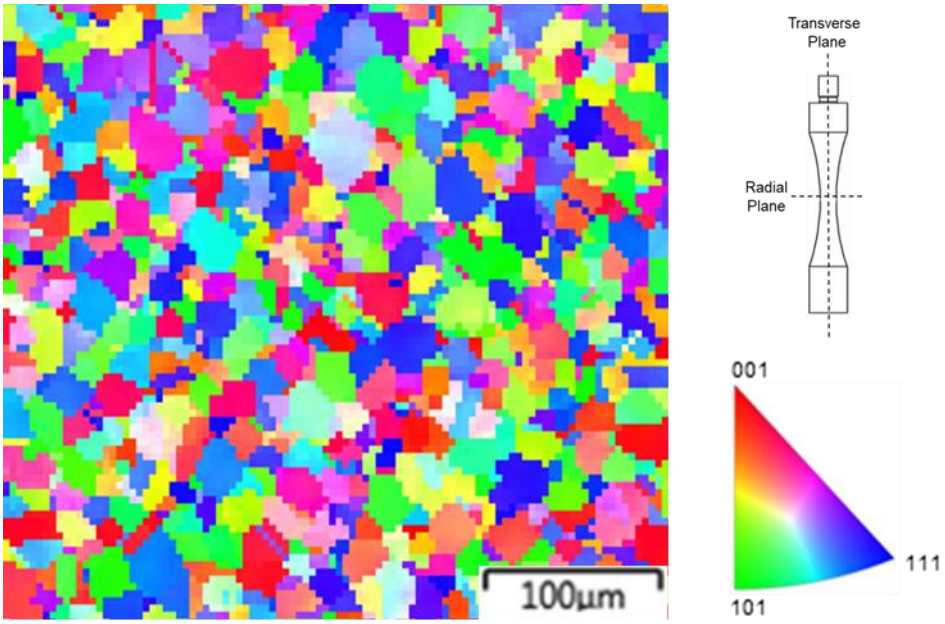

Figure 22. EBSD IPF-Z representative microstructure of wrought Inconel 718 imaged along the specimen transverse plane.

An EDS map with quantitative analysis, as shown in Figure 23, was performed on the LB-PBF Inconel 718 material. The chemical composition obtained through EDS analysis is shown in Table 4, however these results may not accurately represent the bulk material chemistry.

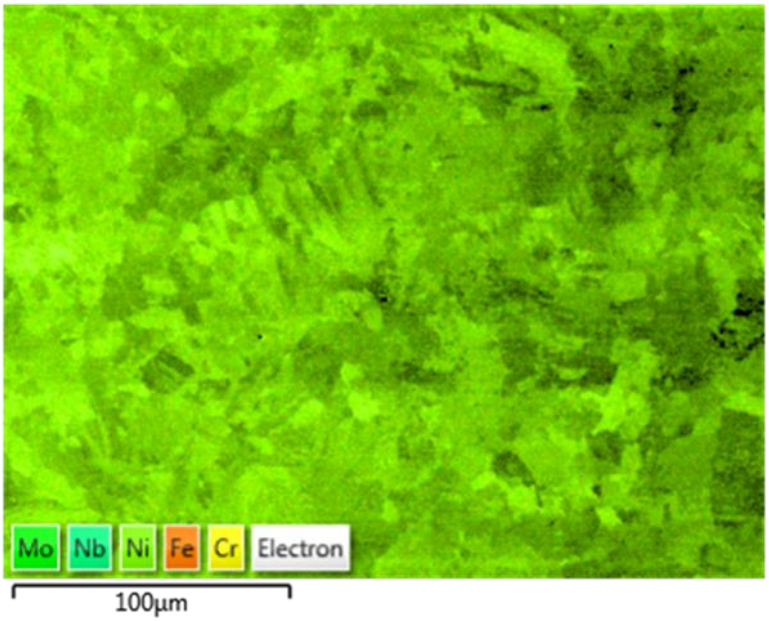

Figure 23. EDS overlaid map of LB-PBF Inconel 718 imaged along the specimen radial plane. The EDS map shows five main elemental constituents: Mo, Nb, Ni, Fe, and Cr.

Table 4. Overall chemistry of LB-PBF Inconel 718 obtained via EDS analysis.

Element	Weight %
Ni	49.2
Nb	5.4
C	5.9
Fe	17.1
Ti	1
Mo	3.1
Cr	18.2

BSE micrographs of LB-PBF Inconel 718 are presented in Figure 24. As-fabricated LB-PBF Inconel 718 microstructures contain a dendritic structure with micro-segregation of Nb [20, 22]. Remnants of these inter-dendritic structures with Nb rich boundaries (determined through EDS line-scan analysis of the regions), which appear as white under SEM, are still apparent in the post-process heat treated LB-PBF Inconel 718 microstructure. Based on the literature [17, 22, 24, 25, 45, 46], the Nb rich, dendritic boundaries are believed to have mostly transformed to γ" precipitates after the heat treatment, however this cannot be concluded for the LB-PBF micrographs in Figure 24 without the use of additional characterization techniques such as x-ray diffraction or transmission electron microscopy. It is, however, unclear if and how much of the Lave phase remains in the inter-dendritic regions.

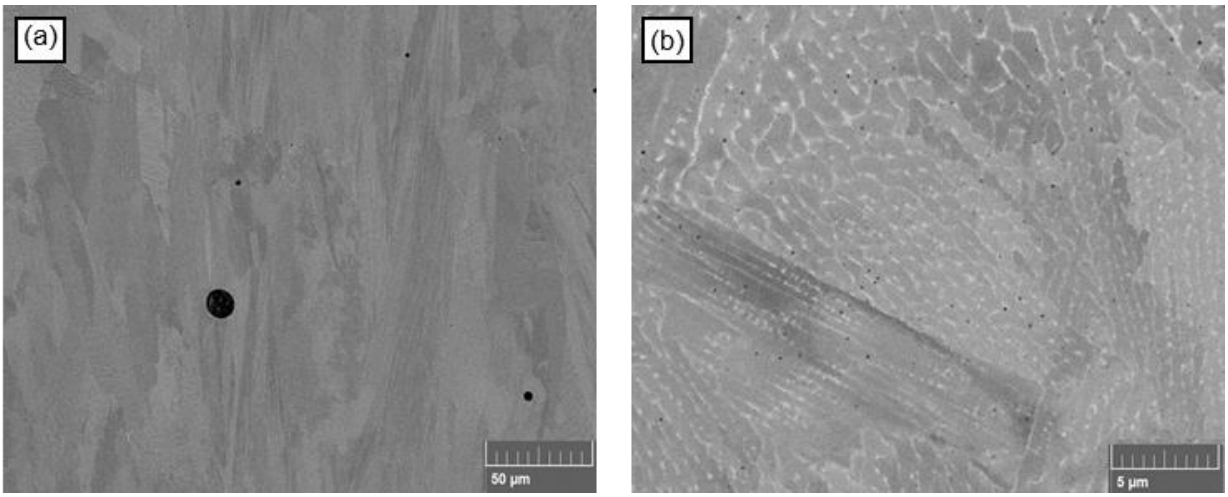

Figure 24. Transverse plane BSE micrographs of LB-PBF Inconel 718 showing (a) columnar grain growth. The magnified image in (b) shows the sub-granular segregation of Nb, which are remnants of the as-fabricated microstructure (without heat treatment). In (b), the Nb structures are white in appearance.

A typical microstructure in the transverse and radial planes of both V and D specimens obtained via EBSD analysis is shown in Figure 25. The microstructure of LB-PBF Inconel 718 shows directional dependent grain growth, characterized as columnar in appearance, where grains are elongated in the direction perpendicular to the build plate. In V oriented specimens, grains are elongated along the loading direction, whereas with D oriented specimens, grains are inclined at 45 degrees with respect to the loading direction. The longitudinal inverse pole figure (IPF) maps from EBSD analysis of specimens of both build layer orientations reveal a scatter in crystallographic orientations, where neighboring grains are separated by high angle grain boundaries (>15 degrees). All grains, regardless of size and shape, contain columnar sub-granular structures with Nb rich boundaries. In Figure 24(a), it is evident that these columnar structures are distinct from sub-grains in the conventional sense (such as ones formed during cold working) as individual columns do not possess distinct orientation. Rather, a “colony” of columns appear to share the same orientation.

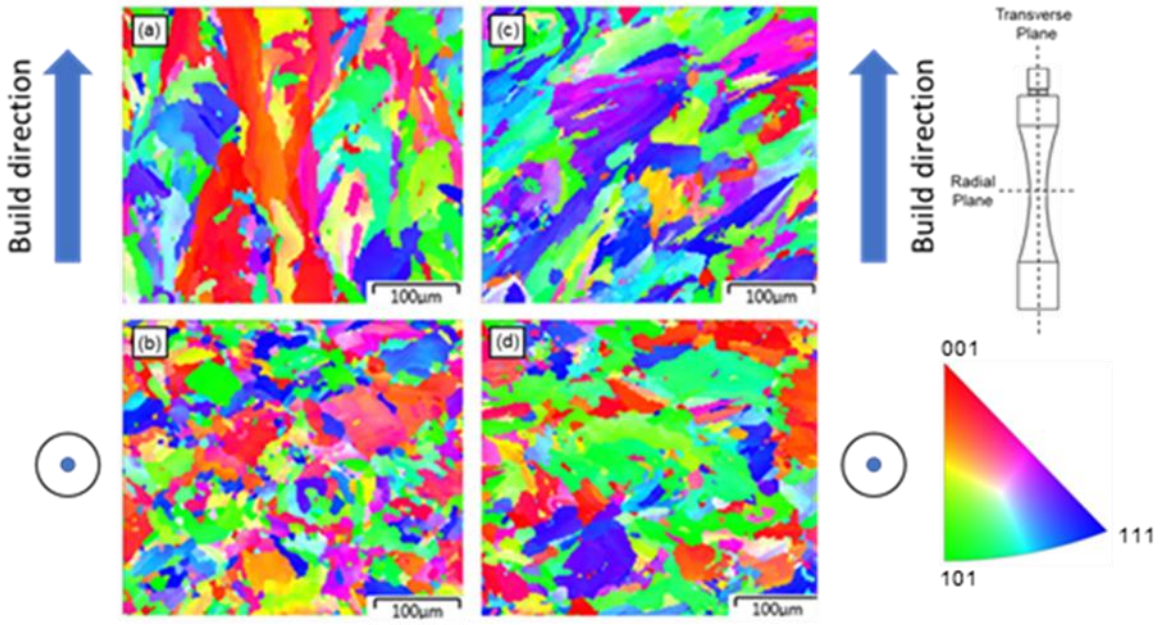

Figure 25. EBSD IPF-Z microstructures of LB-PBF Inconel 718 in (a) transverse and (b) radial planes of a V built specimen, and (c) transverse and (d) radial planes of a D built specimen.

The average grain size observed from the radial plane EBSD maps in Figure 24 is ~11.4 µm for the V specimen and ~12.7 µm for the D specimen. The LB-PBF Inconel 718 microstructure shown in Figure 24 and Figure 25 differ from the wrought material microstructures presented in Figure 21 and Figure 22. For the wrought material used in this study, the average grain size is ~19 µm, which is slightly larger than both LB-PBF specimen types. The LB-PBF Inconel 718 microstructure shows grains that are elongated in the build direction which can potentially result in some level of anisotropy in mechanical properties. Additionally, the LB-PBF material has less apparent intergranular precipitation (γ" and δ phases), instead its secondary phases are in the form of Nb-rich, sub-granular dendritic structures. One commonality, however, is the presence of titanium carbide precipitates. Figure 26 shows a BSE image obtained from the transverse plane of a V oriented LB-PBF Inconel 718 microstructure.

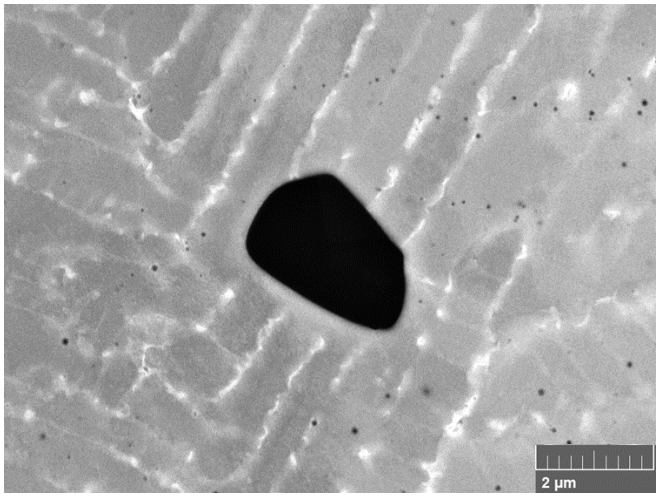

Figure 26. Transverse plane BSE image of a titanium carbide precipitate in a V oriented LB-PBF Inconel 718 sample.

The influence of the as-built surface on resistance fatigue crack initiation was investigated by comparing results of as-built specimen S-N data to that the S-N data of post-process machined samples. The V as-built specimen, as shown in Figure 27, displays the best surface quality of the two build conditions. It is worth noting that as-built surfaces are covered in un-sintered powder particles. The presence of un-sintered particles can greatly affect the standard deviation of R_a values, however, the typical value of R_a for as-built V specimens is expected to be about 3.4 µm.

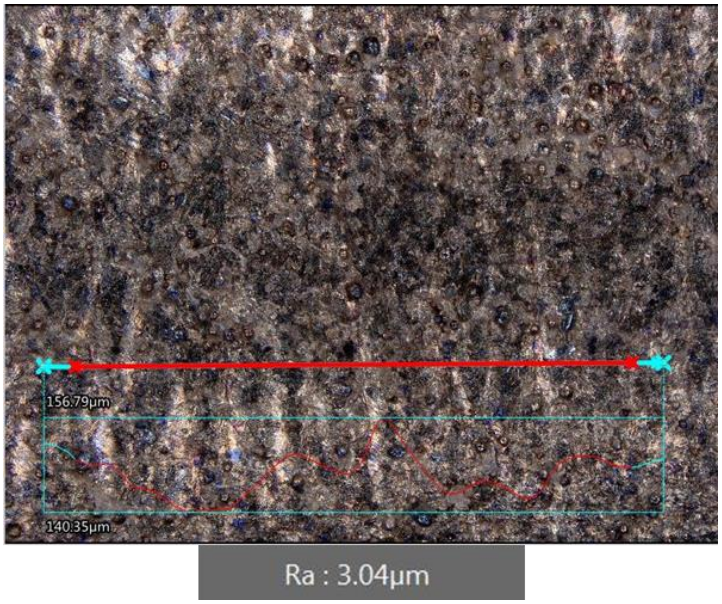

Figure 27. Surface profile and subsequent Ra measurement for the gauge section of an as-built V Inconel 718 test specimen.

It was observed that the as-built D specimen batch exhibited inferior surface quality as compared to the as-built V specimens. It was noted that one distinct region of the exterior of an as-built D specimen, named the *down-skin* surface, contains the roughest surface with a large presence of un-sintered powder particles. The average roughness was calculated on four regions of the specimen exterior: the up-skin (180 degrees offset from down-skin), down-skin, and two sides. Figure 28 shows the noticeable difference in surface quality of the down-skin surface as compared to the other three surfaces shown.

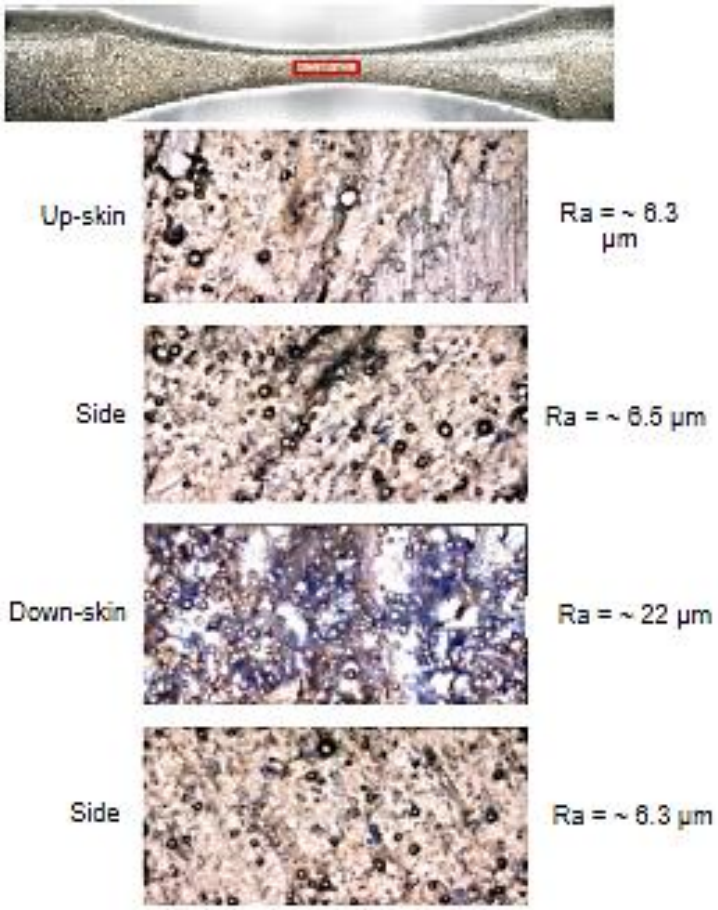

Figure 28. Surface roughness, Ra, measurements of four sides of an as-built D Inconel 718 specimen gauge section.

The down-skin surface has an average roughness of around 22 µm, as compared to the 6.3-6.5 µm average roughness of the remaining three surfaces. Due to the presence of large un-sintered particle clusters, drooping melt pools, and sharp micro-notches, it is expected that fatigue cracks are most likely to initiate from the down-skin surface. Fractography analysis of as-built specimens will be discussed in a later section of this report.

4.2. Fatigue behavior

The S-N data of wrought Inconel 718 specimens are presented in Figure 28. The wrought material data in Figure 29 shows two specimen runout tests at a life of 2 x 10^9 reversals. The fatigue limit that corresponds to this life is between σ_w = 475 – 500 MPa. Since the slope of the S-N curve is not constant along the transition of HCF regime to VHCF regime, the Basquin equation was not suitable for modelling the fatigue behavior of this wrought specimen batch.

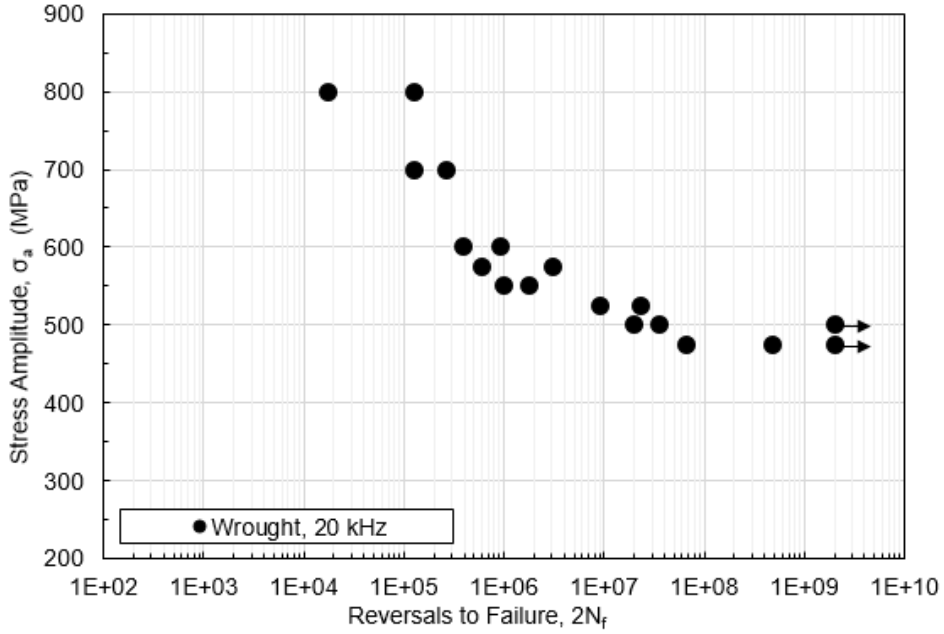

Figure 29. S-N plots for wrought Inconel 718.

The S-N behaviors of post-process machined V and D oriented LB-PBF specimens are presented in Figure 30. Both S-N curves in Figure 30 (a)-(b) show very little change in slope, as represented by the Basquin dashed trendlines. Both V and D machined LB-PBF specimen batches show higher resistance to fatigue failure in the HCF regime (fatigue lives less than 10^7 to 2 x 10^7 reversals). Formulas for the S-N curves of Figure 30 are as follows:

$$\sigma_a = 3584\ N_f{}^{-0.11} \quad \text{for machined V oriented LB-PBF Inconel 718} \tag{6}$$

$$\sigma_a = 3989.5\ {N_f}^{-0.132} \text{ for machined D oriented LB-PBF Inconel 718} \quad (7)$$

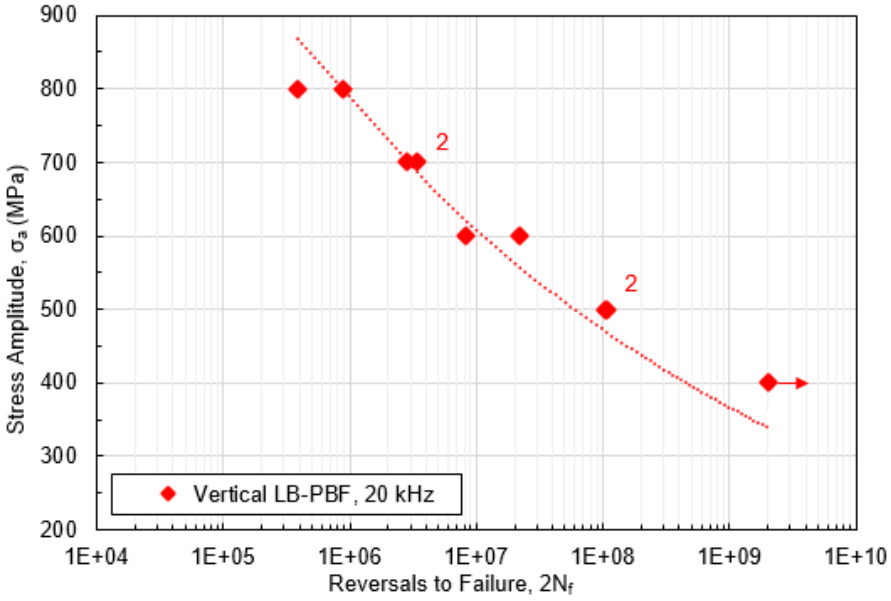

(a)

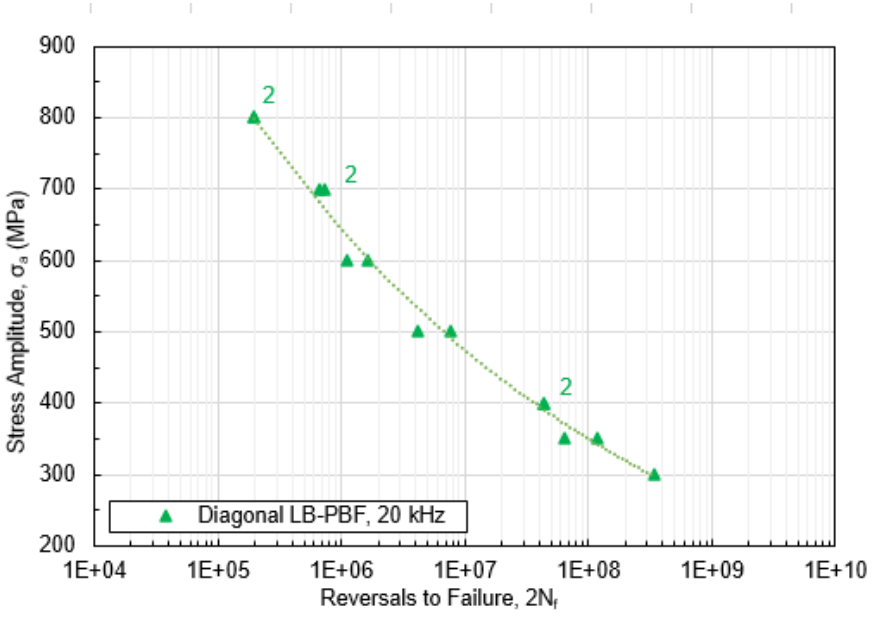

(b)

Figure 30. S-N plots for post-process machined LB-PBF Inconel 718 fabricated in the (a) V and (b) D orientations.

Runout tests were achieved for both the wrought material (Figure 29) and machined V LB-PBF material (Figure 30(a)). These tests correspond to the material fatigue limit, σ_a, at 10^9 cycles or at 2 x 10^9 reversals. The machined V LB-PBF condition yielded a value of σ_a, that closely matches that of the wrought material. Additionally, both the machined V and D LB-PBF conditions showed higher resistance to HCF failure, according to their S-N data.

The S-N behavior of as-built V and D oriented LB-PBF Inconel 718 is reported in Figure 31. The as-built surface condition in LB-PBF parts is more likely to have detrimental effects on mechanical properties as compared to a machined surface. Since LB-PBF is a layer-wise process, surface quality is affected by the build direction: V build orientations result in a superior surface finish as compared to orientations that are inclined to the z direction.

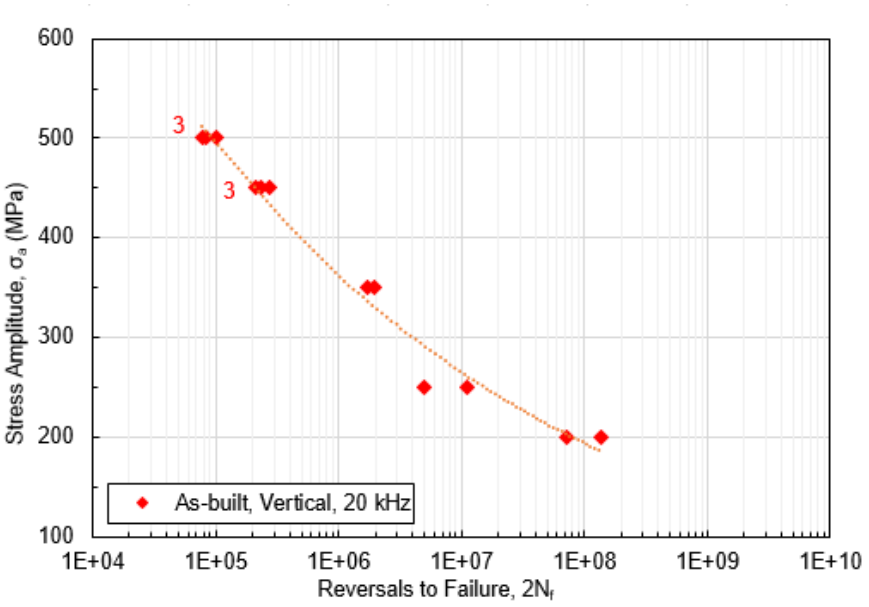

(a)

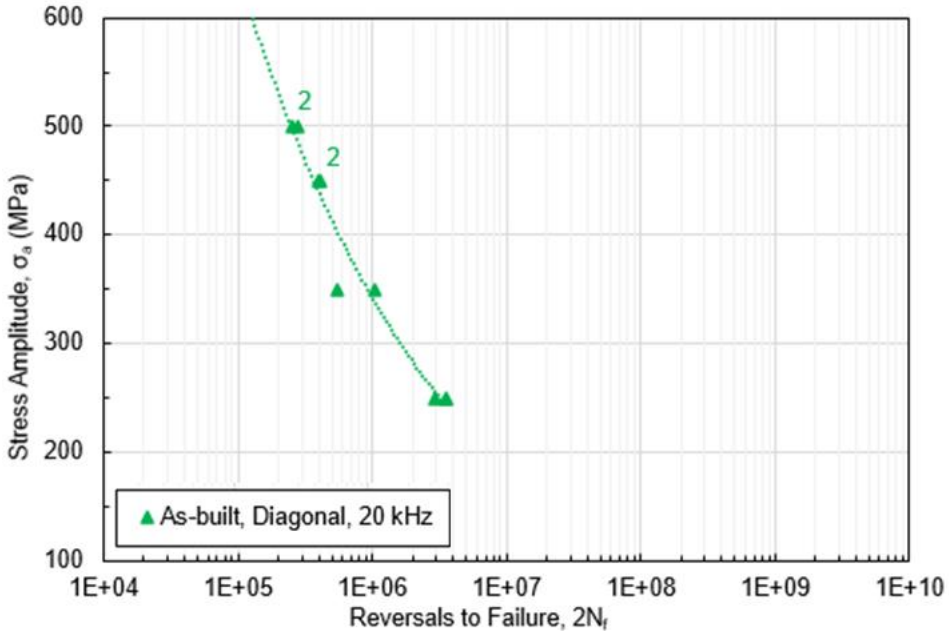

(b)

Figure 31. S-N plots for as-built LB-PBF Inconel 718 fabricated in the (a) V and (b) D orientations.

As expected, the as-built V LB-PBF Inconel 718 specimens experienced fatigue lives that were near three orders of magnitude shorter than their machined AM counterparts. The as-build D condition showed only a 1-2 order of magnitude difference in fatigue lives at each stress amplitude. No VHCF failures (tests exceeding 10^7 cycles of 2 x 10^9 reversals) were recorded for the as-built D condition, however, two VHCF failures did occur for the as-built V condition. Similar to the results in Figure 30, the S-N curves in Figure 31 (a)-(b) show very little change in slope between fatigue regimes. Formulas for the S-N curves of Figure 31 are as follows:

$$\sigma_a = 2360.5\ {N_f}^{-0.136} \text{ for as-built V oriented LB-PBF Inconel 718} \quad (8)$$

$$\sigma_a = 2324.3\ {N_f}^{-0.135} \text{ for as-built D oriented LB-PBF Inconel 718} \quad (9)$$

5. Discussions

5.1. Fractography analysis

5.1.1. Wrought Inconel 718

Following wrought material fatigue tests, specimen fracture surfaces were examined via SEM. Fatigue behavior, including crack initiation mechanisms and fatigue life, was influenced by the stress amplitude, σ_a. It was observed that the main cause of fatigue failure for wrought Inconel 718 was crack initiation and advancement from the specimen surface. In some cases, fatigue cracks were able to initiate from multiple surface sites. An example of this phenomenon is shown in Figure 32. This specimen two distinct large fatigue cracks. The red arrows in Figure 30(a) represent the main crack initiation regions. This type of behavior is characteristic of higher stresses that result in more localized plastic deformation, which aids in formation of multiple surface cracks.

The rotated specimen image shown in Figure 32(b) illustrates that the crack growth occurs radially from a single surface site.

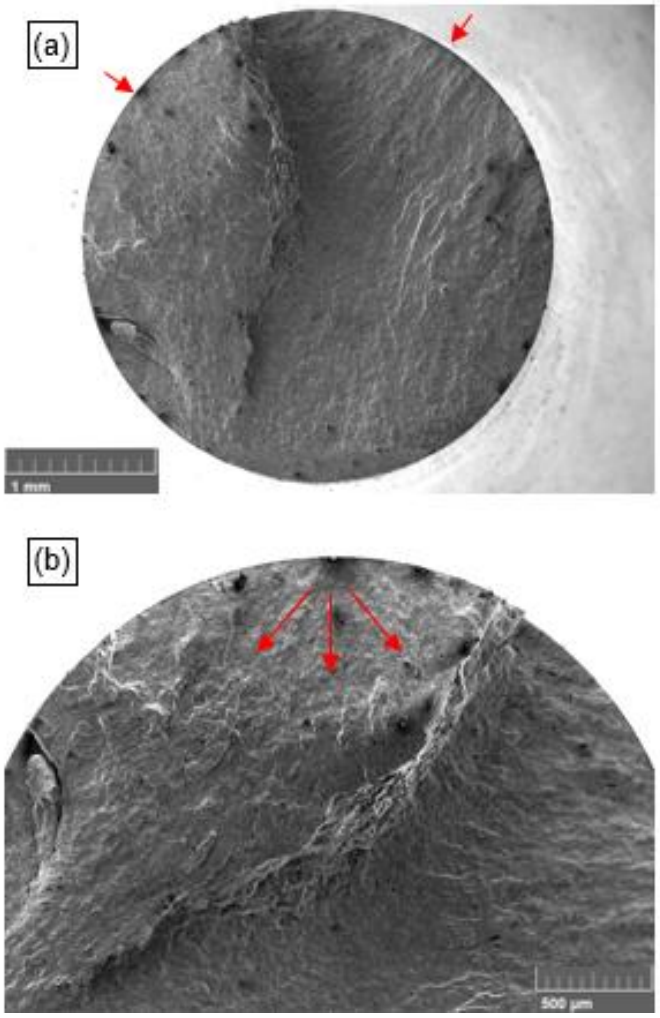

Figure 32. SE fracture surface images of a wrought Inconel 718 specimen tested at σ_a = 700 MPa with a corresponding fatigue life of $2N_f = 1.26 \times 10^5$ reversals. The overall fracture surface is presented in (a) with red arrows pointing to crack initiation sites. One of two crack initiation sites is highlighted in (b).

As σ_a is decreased, the specimen's resistance to localized plastic deformation is increased, however surface fatigue crack initiation is still inevitable. The fractured specimen shown in Figure 33 displays only a single crack initiation site and has experienced fatigue failure in the VHCF regime. In the late stages of the HCF regime, as well as early stages of the VHCF regime,

specimens are expected to fail from cracks that form on the surface or just below [19, 34]. The overload failure and crack growth regions are highlighted in Figure 33(a). The large crack in Figure 33(b) is similar in appearance to the cracks shown in Figure 32.

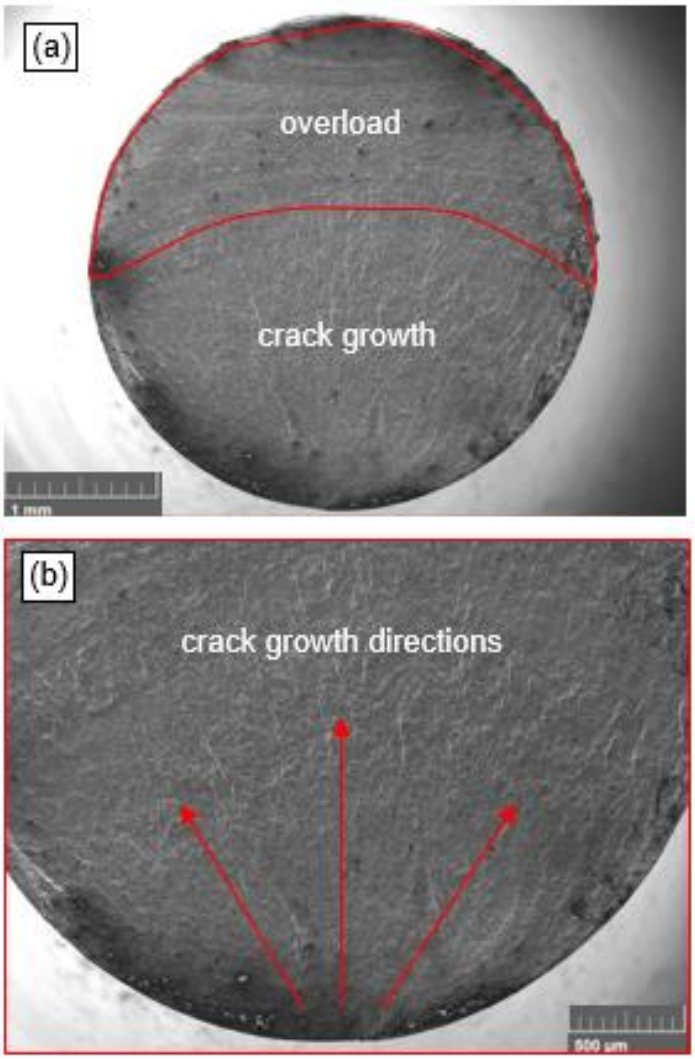

Figure 33. SE fracture surface images of a wrought Inconel 718 specimen tested at σ_a = 500 MPa with a corresponding fatigue life of $2N_f = 2.54 \times 10^7$ reversals. The overall fracture surface with a single crack initiation site is presented in (a). The magnified image in (b) shows the direction of crack growth from the specimen surface.

Wrought Inconel 718 VHCF failures can also stem from sub-surface cracks, such as the one shown in Figure 34. At lower σ_a values, specimen fatigue life is heavily dependent on flaws within the material. Crack initiation typically begins from a sub-surface microstructural flaw such as an abnormally large grain or brittle particles [34]. This type of fracture is referred to as a fisheye fracture, as the optical appearance of the fracture surface resembles a fisheye [47]. Unlike what was seen for the specimens in Figure 32 and Figure 33, the crack growth region in Figure 34(b) shows clearly defined fatigue striations.

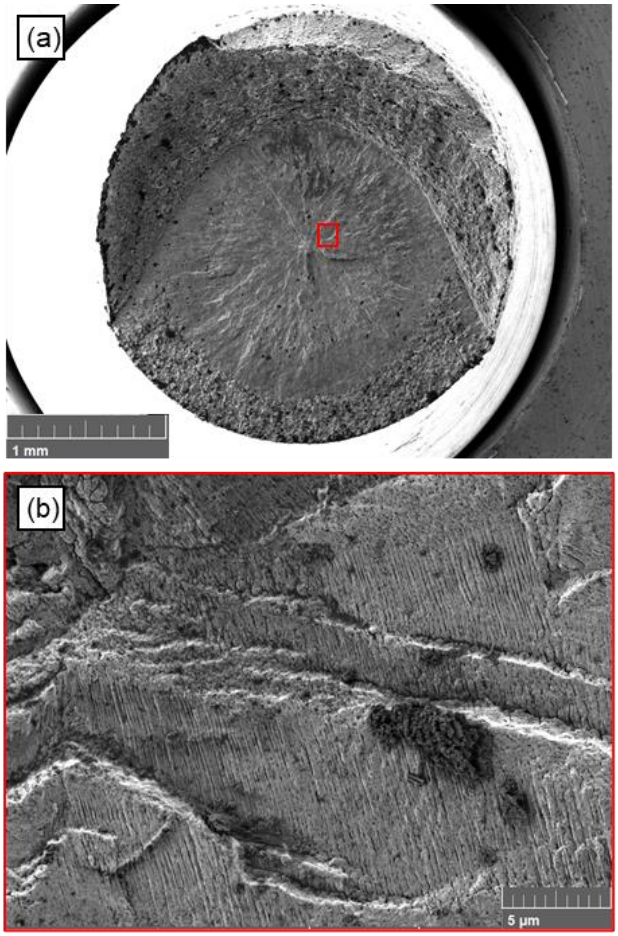

Figure 34. SE fracture surface images of wrought Inconel 718 specimen tested at σ_a = 550 MPa with a corresponding fatigue life of $2N_f = 5.94 \times 10^7$ reversals. The overall fracture surface in (a) shows a single, internal crack initiation site with (b) trans-granular crack growth showing fine fatigue striations.

5.1.2. LB-PBF Inconel 718 in machined surface finish condition

The analysis of machined LB-PBF Inconel 718 specimens revealed a HCF failure mode similar to the results shown for wrought Inconel 718. Based on numerous literature reports [5, 9, 13, 30-33, 35, 42, 48-51] that illustrate the role of process induced defects in the fatigue resistance of AM metals, the LB-PBF material was expected to initiate fatigue cracks at the weakest links in the microstructure. The fractured machined V specimen shown in Figure 35 did not display fatigue crack initiation due to process induced defects. Rather, the fatigue crack initiated due to surface slip without the presence of apparent defects. Additionally, the fatigue crack initiated from a single site rather than multiple sites.

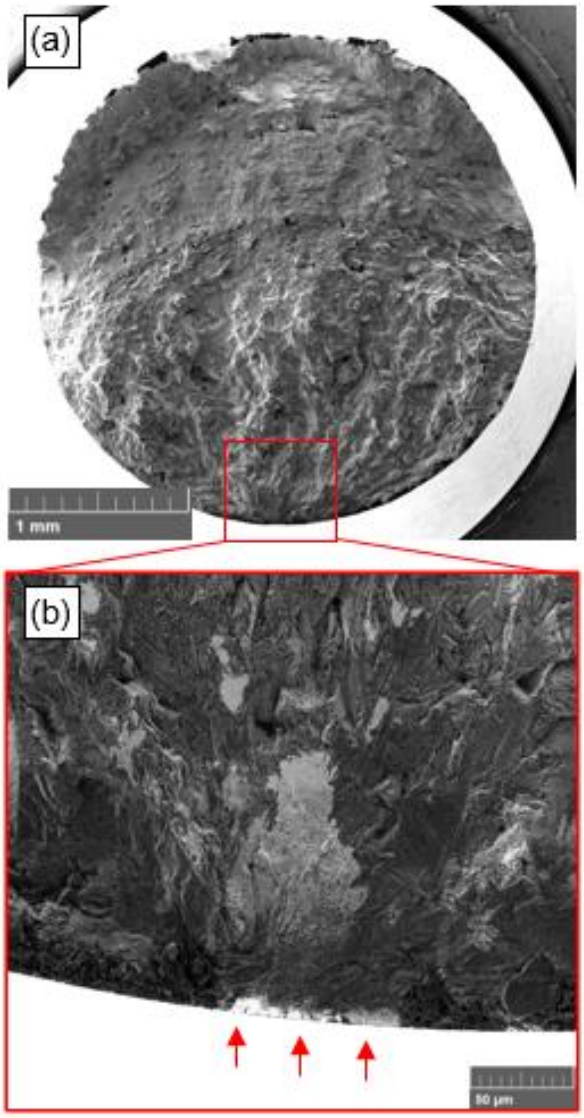

Figure 35. SE fracture surface images a machined V LB-PBF Inconel 718 specimen tested at σ_a = 800 MPa with a corresponding fatigue life of $2N_f = 3.89 \times 10^5$ reversals. The overall fracture surface in (a) shows a single crack initiation site, which is magnified in (b).

In a similar manner to what was observed for wrought Inconel 718, decreased σ_a led to a shift from surface fatigue crack initiation to a sub-surface crack initiation mode. It is apparent in Figure 36(a) that there is no distinct crack growth region. The overall fracture surface is torturous in appearance. This type of result is typically observed when a fatigue failure results from multiple

fatigue cracks. Additionally, this type of fatigue failure is difficult to trace since fatigue crack growth is occurring in multiple directions. A possible crack initiation site for this specimen is a process induced defect shown in Figure 36(b). The defect in the case of Figure 36(b) is a large entrapped gas pore.

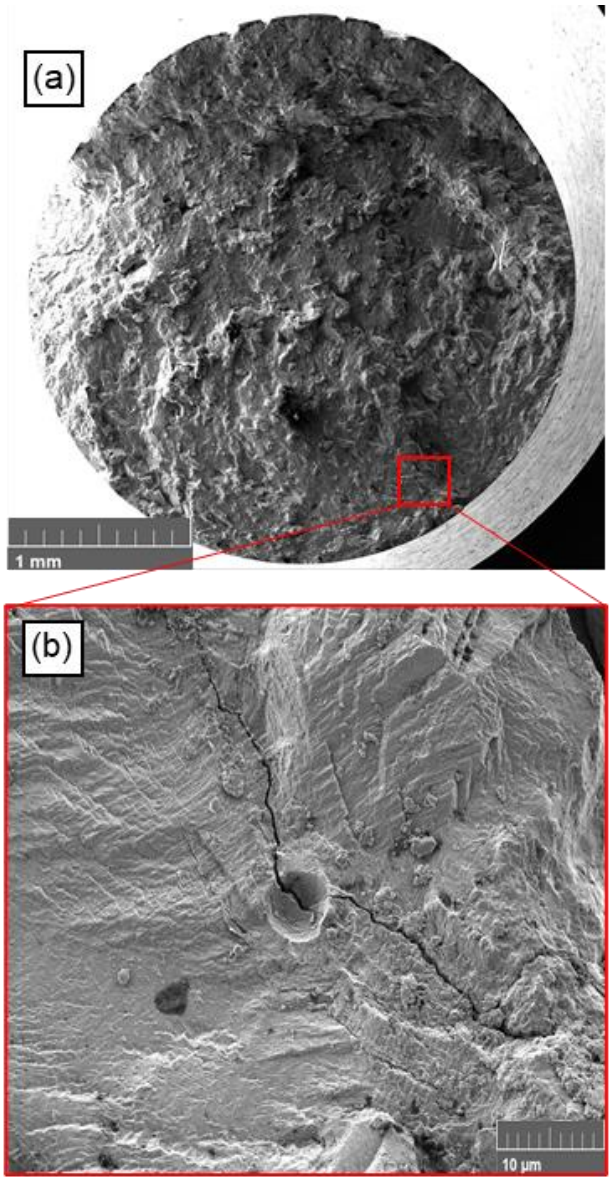

Figure 36. SE fracture surface images of a machined V LB-PBF Inconel 718 specimen tested at σ_a = 500 MPa with a corresponding fatigue life of $2N_f = 1.04 \times 10^8$ reversals. The overall fracture surface in (a) presents the possibility of multiple crack initiation sites, such as the remnant of an entrapped gas pore shown in (b).

For the HCF regime fractures of machined D LB-PBF specimens, it was observed that the main cause of fatigue failure was surface crack initiation. D machined LB-PBF specimens, such as the one shown in Figure 37, showed signs of multiple surface crack initiation sites. An example of an overserved surface crack initiation site for this specimen is shown in Figure 37(b). Similar to the overall fracture surface shown in Figure 36(a), the fractured specimen in Figure 37 contained a torturous fracture path, which is characteristic of multiple coalescing fatigue cracks. The specimen was tilted in Figure 37(b) in order to show one of the possible crack initiation sites. Additionally, the morphology of the crack initiation site does not appear to be influenced by nearby AM process induced defects, such as LoF or entrapped gas porosity.

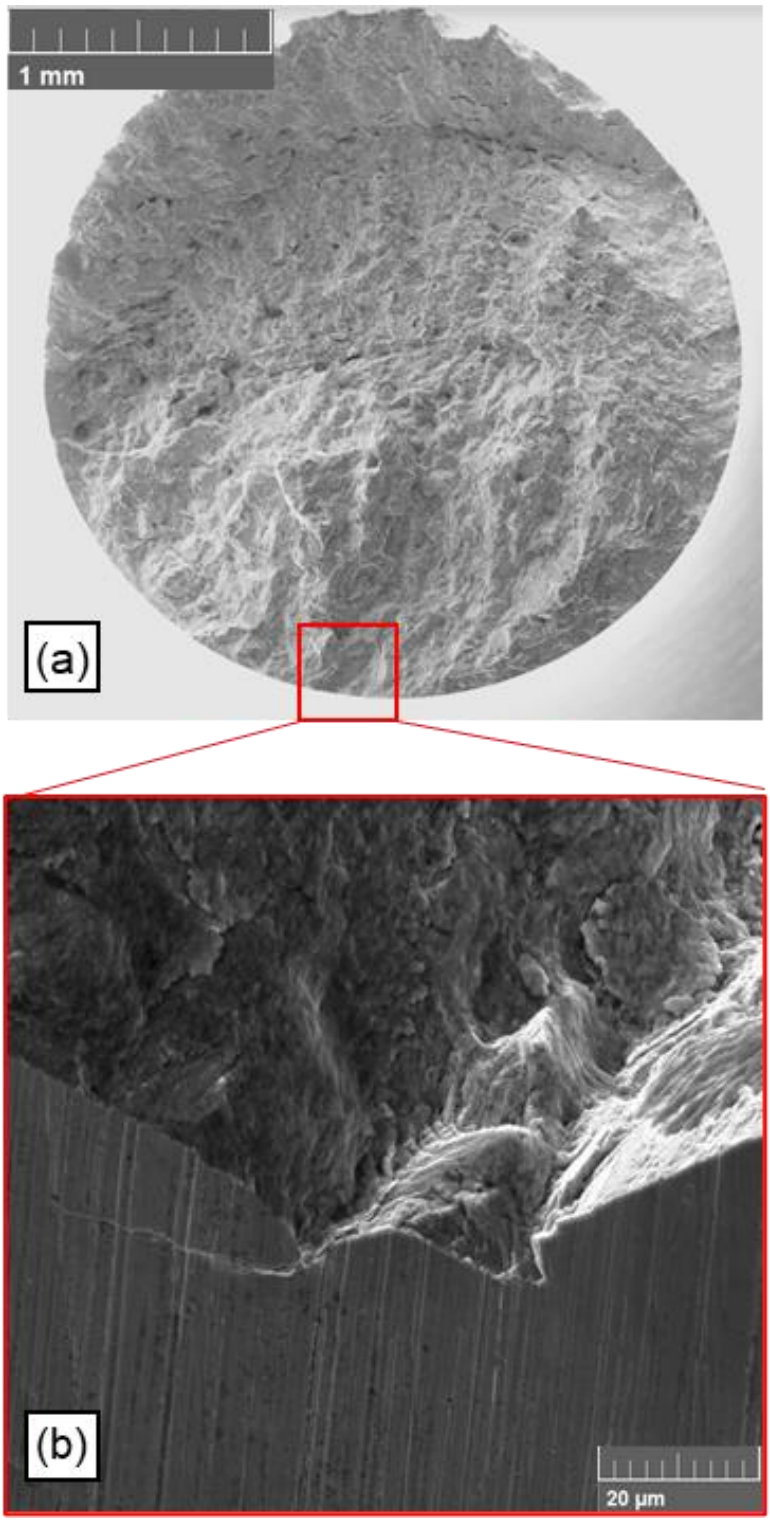

Figure 37. SE fracture surface images of a machined D LB-PBF Inconel 718 specimen tested at σ_a = 700 MPa with a corresponding fatigue life of $2N_f = 6.76 \times 10^5$ reversals. The specimen in (a) experienced surface crack initiation from multiple sites, such as (b).

A different type of crack initiation mechanism was observed in the machined D LB-PBF specimen shown in Figure 38. The overall fracture surface in Figure 38(a) shows no distinct crack growth regions, which again presents the possibility of multiple crack initiation sites, such as the ones shown in Figure 38 (b)-(c). The mechanism shown in Figure 38 (b)-(c) is not a defect, rather a facet from which fatigue cracks stem. The facets are coherent with the matrix and are not expected to be of a different composition. This type of fracture feature was also observed by [31] in fractured specimens that were free of large process induced defects at the gauge section. This type of failure is believed to occur in matrix grains with favorable orientation and is a similar mode to porosity induced crack initiation [31].

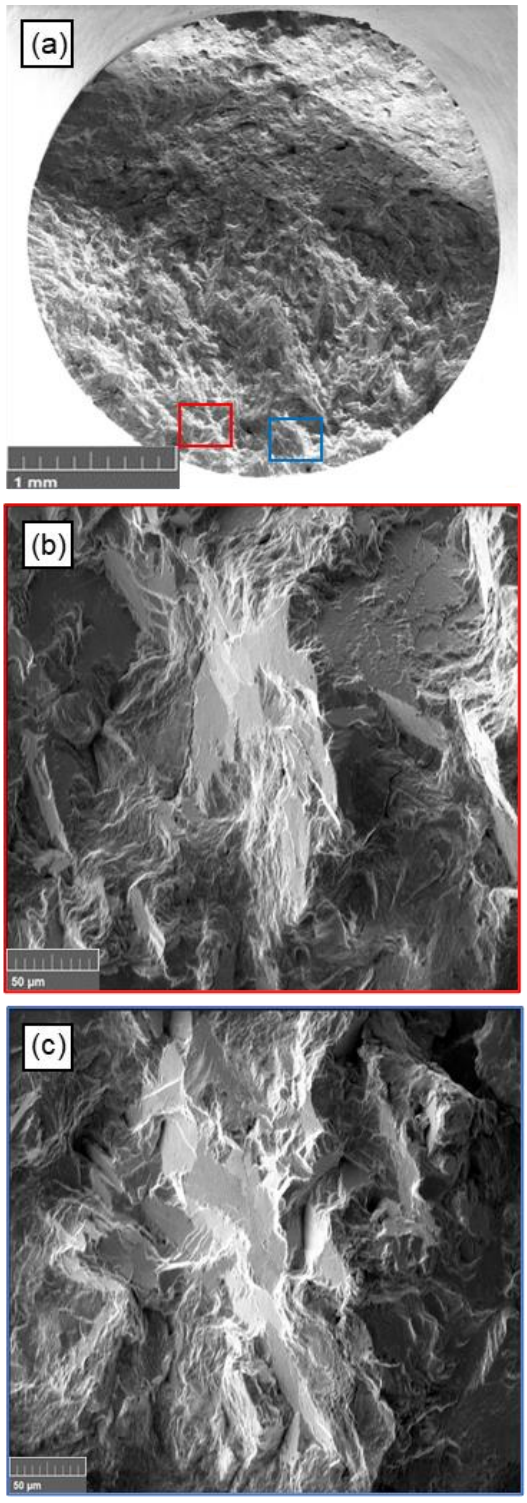

Figure 38. SE fracture surface images of a machined D LB-PBF Inconel 718 specimen tested at σ_a = 500 MPa with a corresponding fatigue life of $2N_f = 7.77 \times 10^6$ reversals. The overall fracture surface in (a) showed the possibility of multiple crack initiation sites. The images (b) and (c) show possible crack origin facets.

5.1.3. LB-PBF Inconel 718 in as-built surface finish condition

For the as-built LB-PBF condition, fatigue resistance is more influenced by competing failure modes from process induced defects, namely, the poor quality of the as-built surface. In addition to stair-step surfaces, which is illustrated in Figure 13, the quality and consistency of a part's geometry can be negatively influenced by the build process. For instance, the fracture surfaces in Figure 39 and Figure 40 showed a single crack initiation site that stemmed from the specimen surface. There is no LoF defect present at the crack initiation sites shown in Figure 39(b) and Figure 40(b), rather a discontinuity in the concentricity of the circular gauge cross section. Since fatigue crack initiation is typically a competition among the many failure modes (such as surface crack initiation from one site or multiple sites), the defect in this case was a notch that resulted from the poor build quality. Notches act as stress concentration sites, therefore the local stress value at the sites shown in Figure 39(b) and Figure 40(b) was enough to initiate a fatigue crack. It is clear that the notch in Figure 39(b) is "sharper" than the notch in Figure 40(b), which would contribute to reduced fatigue resistance.

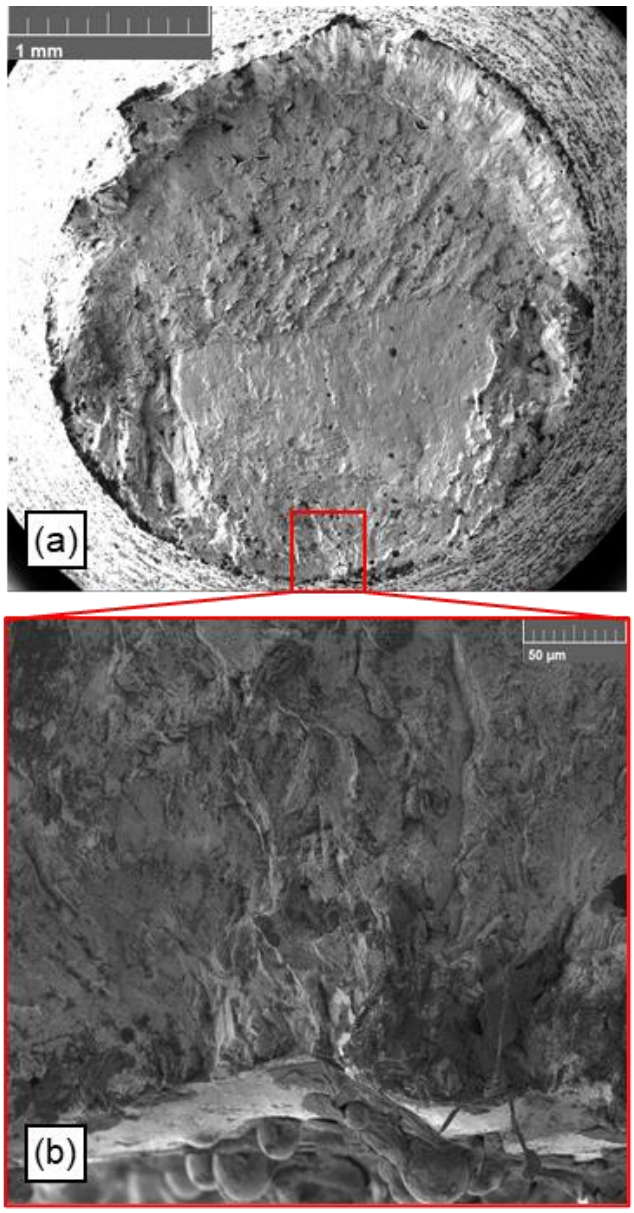

Figure 39. SE fracture surface images of an as-built V LB-PBF Inconel 718 specimen tested at σ_a = 500 MPa with a corresponding fatigue life of $2N_f = 1.02 \times 10^5$ reversals. The as-built V specimen in (a) failed as a result of surface crack initiation, shown in (b). The crack initiating defect was a slight discontinuity in the geometry, which resulted in a notch on the surface.

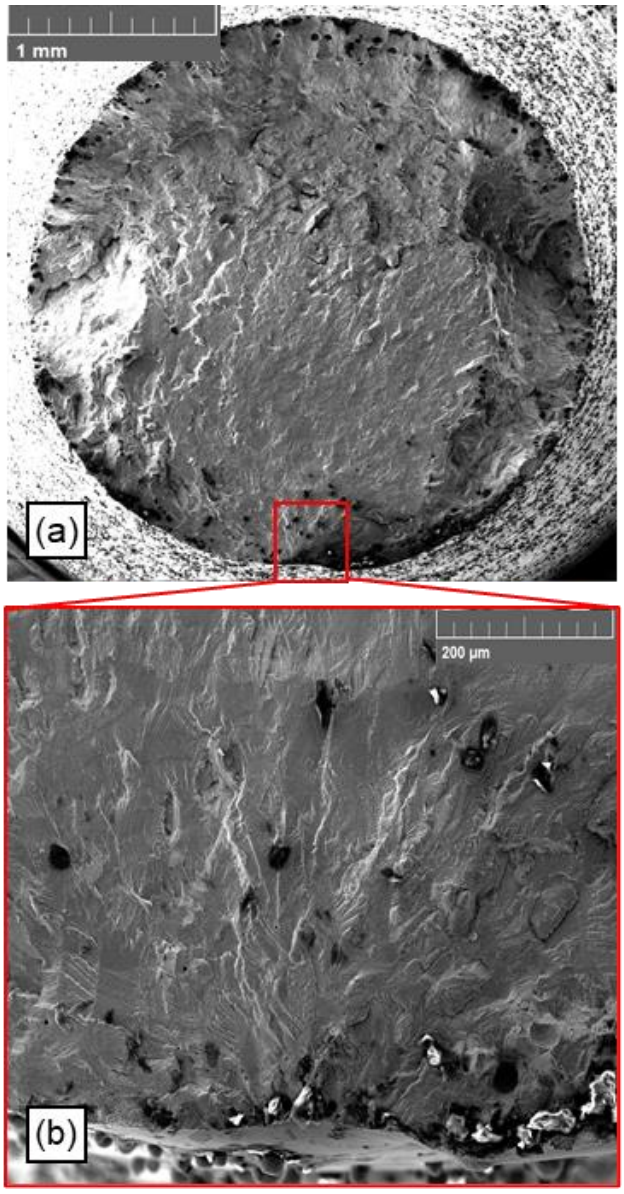

Figure 40. SE fracture surface of an as-built V LB-PBF Inconel 718 specimen tested at σ_a = 350 MPa with a corresponding fatigue life of $2N_f = 1.74 \times 10^6$ reversals. The overall fracture surface is presented in (a). This specimen failed as of a result of a micro-notch on the specimen surface. The crack initiation site is shown in (b).

For the as-built D LB-PBF condition, fatigue resistance was heavily influenced by the poor surface quality, especially from the down-skin surface. Unlike the as-built V specimens in Figure 39 and Figure 40, the as-built D specimen fractures in Figure 41 and Figure 42 showed multiple crack initiation sites. Figure 41 (b)-(c) highlights sources of fatigue crack initiation. Development

of the poor quality down-skin surface during the build process induces sharp surface notches, such as the one shown in Figure 41(b). The down-skin surface quality is a result of melt pool seep through the supporting powder bed, which results in high concentration of surface defects. The morphology of the down-skin surface is highlighted in low and higher magnification images in Figure 42 (b)-(c), respectively. These types of defects cause crack initiation sites like the one shown in Figure 41(c).

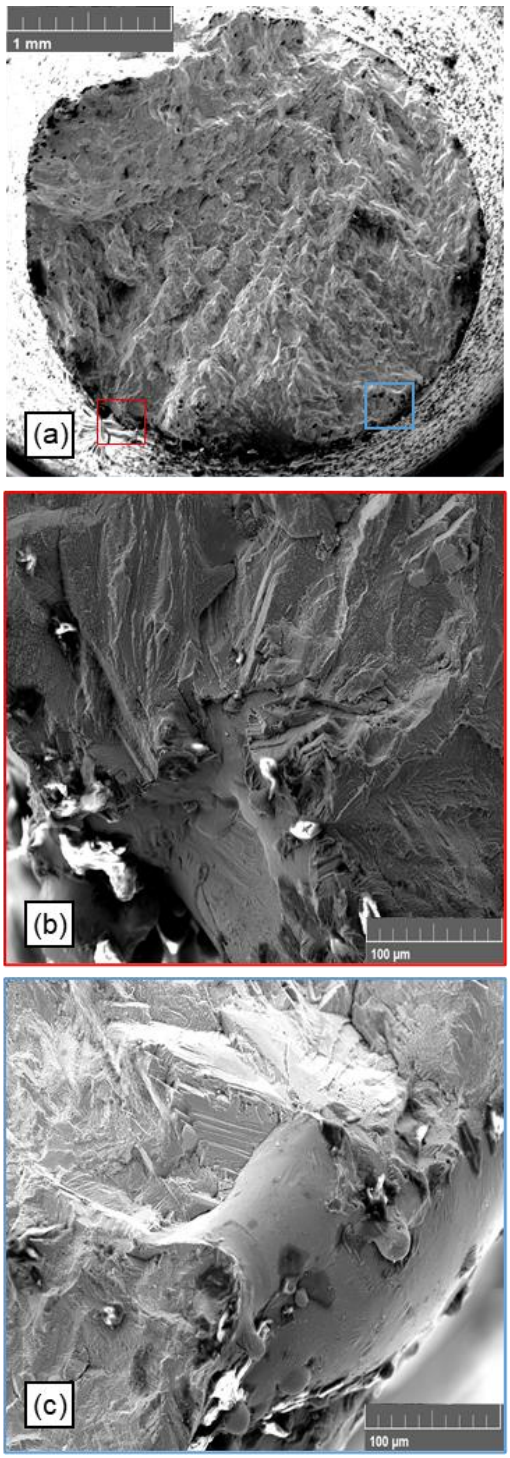

Figure 41. SE fracture surface of an as-built D LB-PBF Inconel 718 specimen tested at σ_a = 500 MPa with a corresponding fatigue life of $2N_f$ = 2.58 x 10^5 reversals. The overall fracture surface in (a) shows a torturous crack path, which is characteristic of fatigue fractures resulting from multiple cracks. Crack initiation sites in this type of specimen (b)-(c) can be in the form of sharp notches or down-skin surface defects.

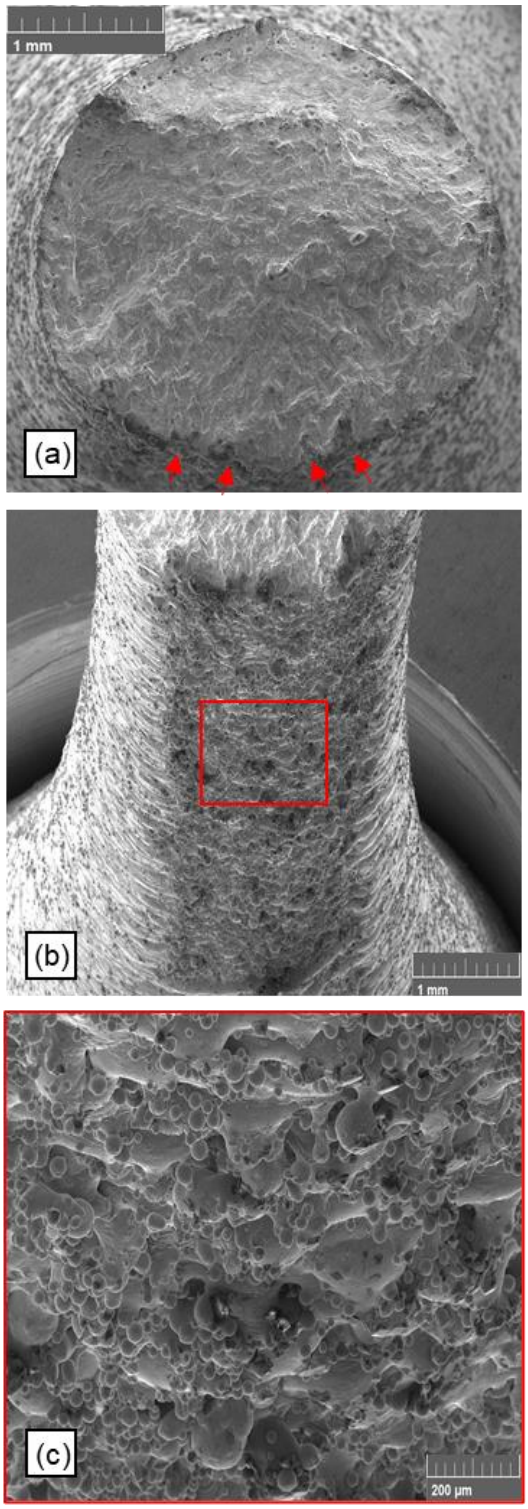

Figure 42. SE fracture surface of an as-built D LB-PBF Inconel 718 specimen tested at σ_a = 350 MPa with a corresponding fatigue life of $2N_f = 5.46 \times 10^5$ reversals. The overall fracture surface in (a) shows cracks originating exclusively from the down-skin surface, shown in (b) and (c).

5.2. Effects of layer orientation on fatigue behavior

The comparisons of the fatigue behavior for V and D LB-PBF IN718 specimens tested in the as-built and machined conditions are displayed in Figure 43 (a)-(b), respectively. The layer orientation effects are apparent in the machined condition than in the as-built condition. For machined specimens built in the V orientation, crack initiation sites were less obvious than for specimens built in the D orientation. SEM imaging of machined V specimens, such as the one shown in Figure 36(b), sub-surface crack initiation appears to be a function of process induced defects, such as large entrapped gas pores. For the case of D oriented specimens, sub-surface cracks appeared to have initiated from multiple faceted regions, such as the ones shown in Figure 38 (b)-(c). The effect of layer orientation was less obvious for HCF regime fractures. In both machined V and machined D build orientations, HCF cracks appeared to have initiated from the surface. Based on the results from fractography, it is more likely that D oriented specimens-initiated cracks from multiple sites on the surface, as compared to the single crack initiation sites observed in the V specimen fractures. It can be best concluded that layer orientation does not directly influence the fatigue resistance of the bulk material; instead, the direction of the parts build-layers influences the failure modes that nucleate fatigue cracks.

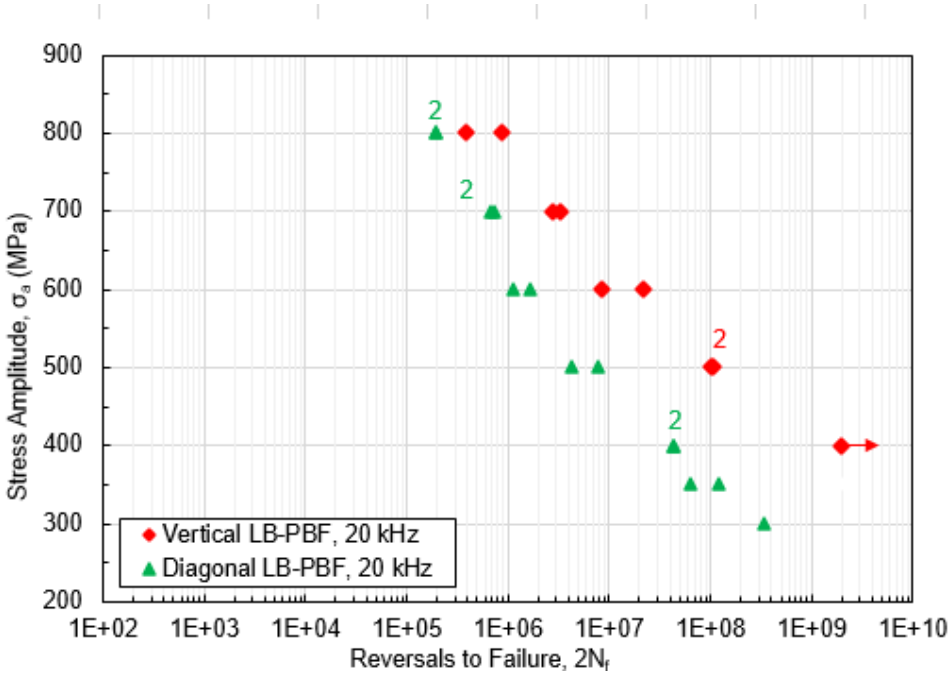

(a)

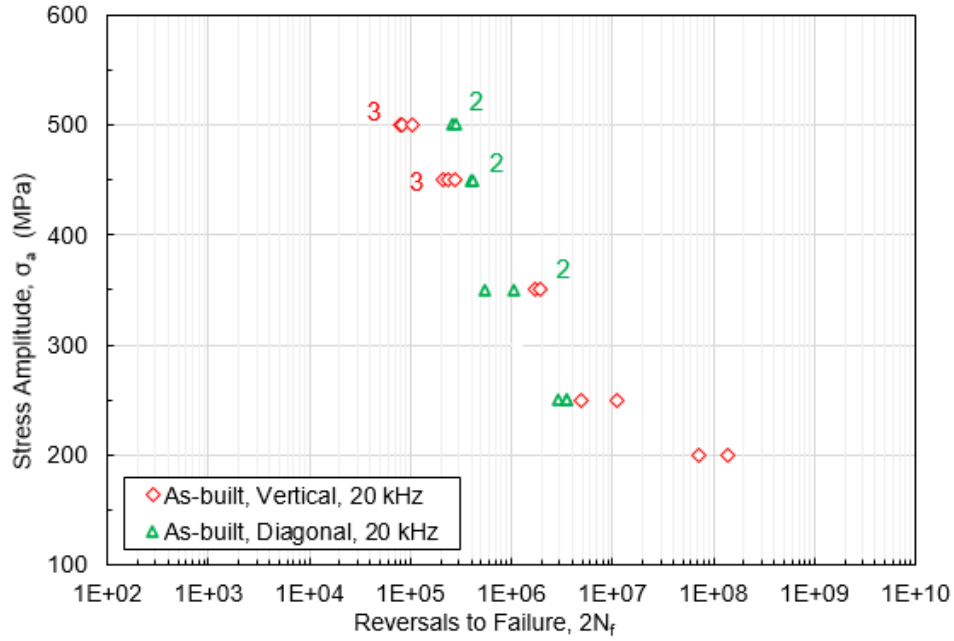

(b)

Figure 43. The effects of build orientation on S-N behavior are shown in (a) for the as-built condition and (b) for the post-process machined condition.

As shown in Figure 43(b), the discrepancy in fatigue behavior between the V and D build layer orientations is not as significant for specimens tested in the as-built surface condition. Despite the fact that as-built D specimens contain a detrimental down-skin surface quality, their fatigue resistance was very similar to the as-built V specimens. In the HCF and VHCF regimes, tests are performed at lower values σ_a. It is known that a larger portion of the total fatigue life spent in the crack propagation stage [26, 47]. As-built D specimens show evidence of multiple fatigue cracks originating from the down-skin surface that coalesce to form one large crack, whereas as-built V specimens initiate a crack from a single flaw on the specimen surface. Since fatigue life of as-built V and as-built D specimens are similar at each stress amplitude, it is impossible to speculate on the effects of layer orientation.

5.3. Effects of surface finish on fatigue behavior

The as-built surface condition in LB-PBF metallic parts is most likely to have detrimental effects on mechanical properties as compared to a machined surface. Since LB-PBF is a layer-wise process, surface quality is affected by the build direction: V build orientations result in superior surface finishes as compared to orientations that are inclined to the z direction.

As-built V specimen surfaces are characterized as having micro-notches resulting from the layer-wise build process. These micro-notches are most likely to initiate a fatigue crack, especially in surface areas with high amounts of un-sintered metallic powder particles. As measured by Keyence profilometry software, as-built V specimens display an average of 3μm surface roughness, which is significantly worse than a machined and polished surface. Furthermore, as-built D specimens contain an extremely poor down-skin surface roughness of ~ 22μm. Poor surface finish in the as-built specimens clearly leads to lower fatigue performance due to increasing

number of crack initiation sites, however the fatigue life discrepancy between the as-built V condition and as-built D condition is negligible.

The influence of surface quality on fatigue life becomes increasingly important in HCF and VHCF, where crack initiation stage dominates the total fatigue life. Figure 44 presents the S-N data for V and D oriented LB-PBF Inconel 718 specimens in both the as-built and machined conditions. Runout tests are indicated with an arrow as shown in this Figure.

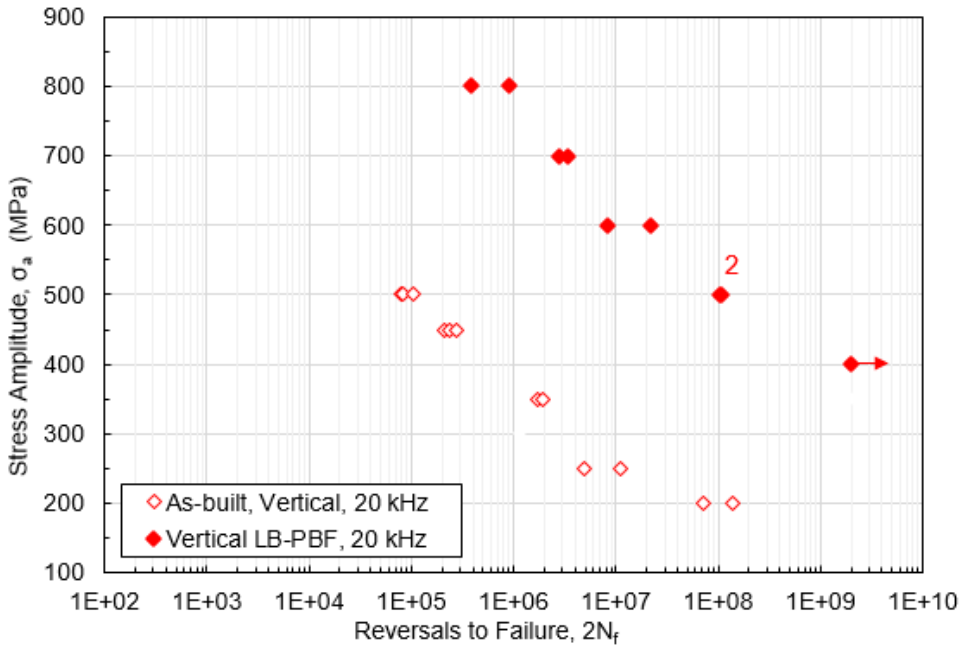

(a)

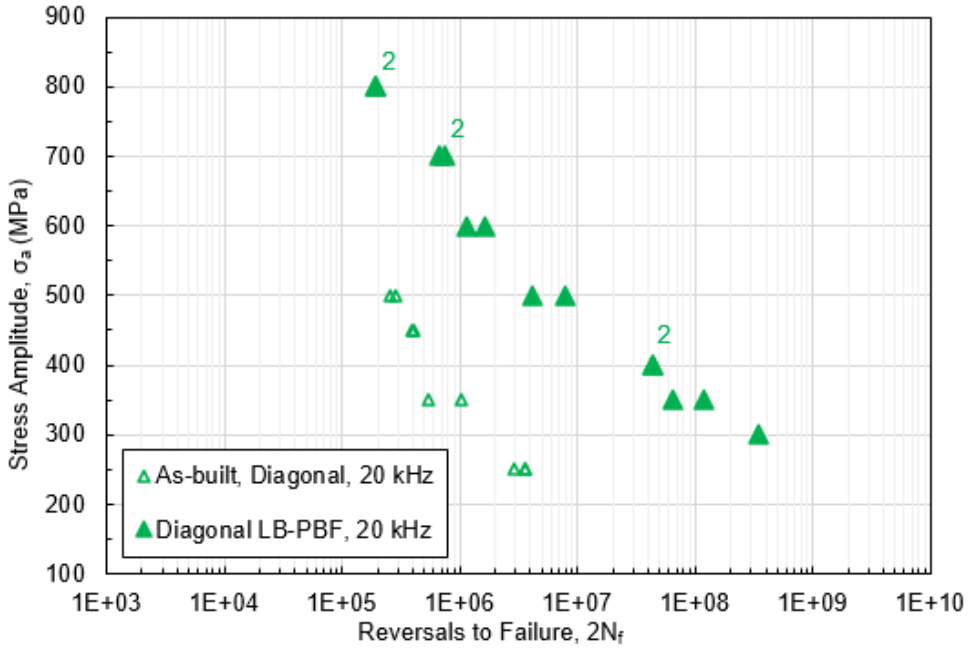

(b)

Figure 44. The effects of surface condition on S-N behavior are shown in (a) for the V build orientation and (b) for the D build orientation.

The effect of the as-built surface condition appears to be greater for the V build direction as compared to the D build direction. D built specimens saw a fatigue life improvement of two orders of magnitude when machined and polished. The purpose of this experiment was to investigate the effects of the as-built surface finish and manufacturing induced defects on the VHCF behavior of LB-PBF Inconel 718 specimens.

The advantage of USF testing is the ability to test fatigue specimens beyond the traditional fatigue limit of 2 x 10^7 reversals in a short amount of time. However, only two as-built t est specimens were able to exceed the 2 x 10^7 reversals threshold. This is due to the limitations imposed by the specimen geometry and the testing equipment available. Based on the specimen geometry and material properties, the USF fatigue test system was only able to produce a minimum stress amplitude of 200 MPa. Only two specimens, from the as-built V specimen batch, were able to exceed the 2 x 10^7 reversal threshold. The results of these fatigue tests will be discussed in the next section.

5.4. Fatigue limit prediction of as-built V Inconel 718 using Murakami's model

As discussed in the previous section, as-built V samples tested at $\sigma_a = 200$ MPa experienced fatigue failure at a number of reversals exceeding 2 x 10^7. These two tests represent the only observed VHCF regime fractures from both the as-built V and as-built D condition. Figure 45 and Figure 46 show the resulting fracture surfaces of the two as-built V samples tests at $\sigma_a = 200$ MPa.

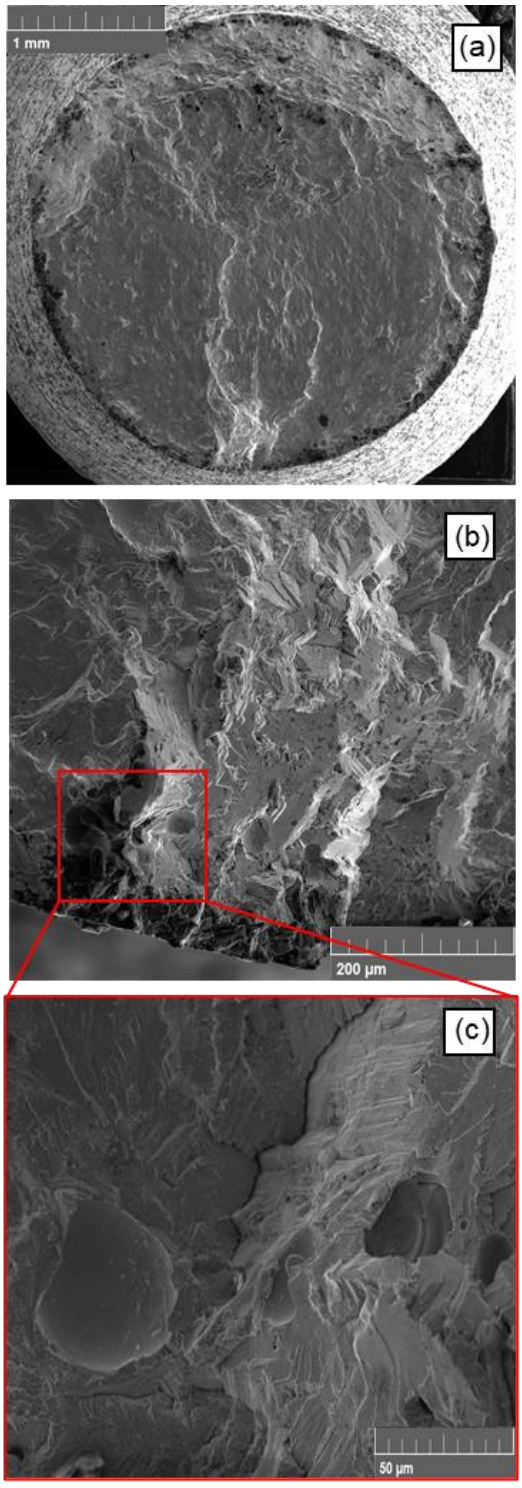

Figure 45. SE fracture of as-built V specimen tested at σ_a = 200 MPa with $2N_f$ = 7.3 x 10^7 reversals. The overall fracture surface is shown in (a) and the magnified crack initiation site is shown in (b).

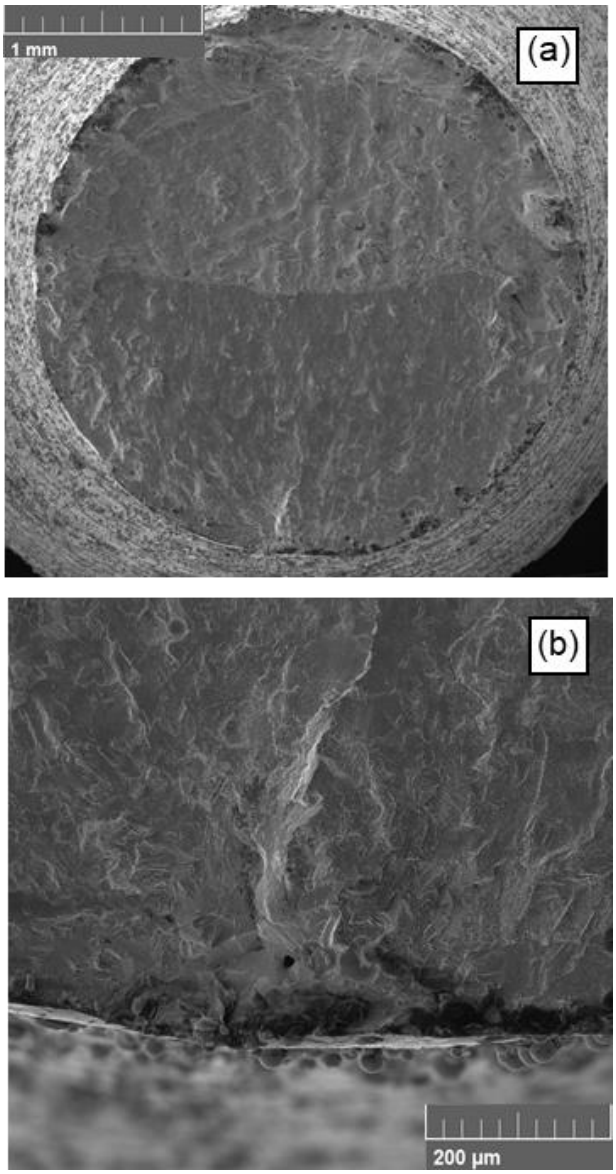

Figure 46. SE fracture of as-built V specimen tested at σ_a = 200 MPa with $2N_f$ = 1.4 x 10^8 reversals. The overall fracture surface is shown in (a) and the magnified crack initiation site is shown in (b).

Both of the fracture surfaces in Figure 45 and Figure 46 show a fracture type that does not seem to originate at a surface flaw. Instead, the crack initiation mechanism appears to be linked to the presence of large sub-surface defects, such as what is shown in Figure 45(c). For all as-built specimens, regardless of build layer orientation, the majority of detrimental process induced

defects existed at a depth of ~100µm below the specimen surfaces. It was observed in [30, 31, 33, 35] that AM metals can experience a failure mode shift from surface crack initiation to sub-surface crack initiation. The overall lack of sub-surface defects at depths exceeding ~100µm below the surface explains the significant improvement of the LB-PBF material's fatigue resistance after post process machining, as these detrimental defects are effectively removed.

Murakami's [27] approach to defect sensitive modelling of a material's fatigue behavior can only apply to fatigue failures that originate from a single fatigue crack. Additionally, this approach can only be utilized if the crack initiation site is a process induced flaw, such as AM defects [19, 27]. Therefore, only the two as-built V VHCF fractures are suitable for σ_w modelling. Fatigue limit was predicted based on the observed crack initiation sites in Figure 45(b) and Figure 46(b). Figure 47 highlights the magnified crack initiation sites from these two specimens as well as depicts the proposed defect area.

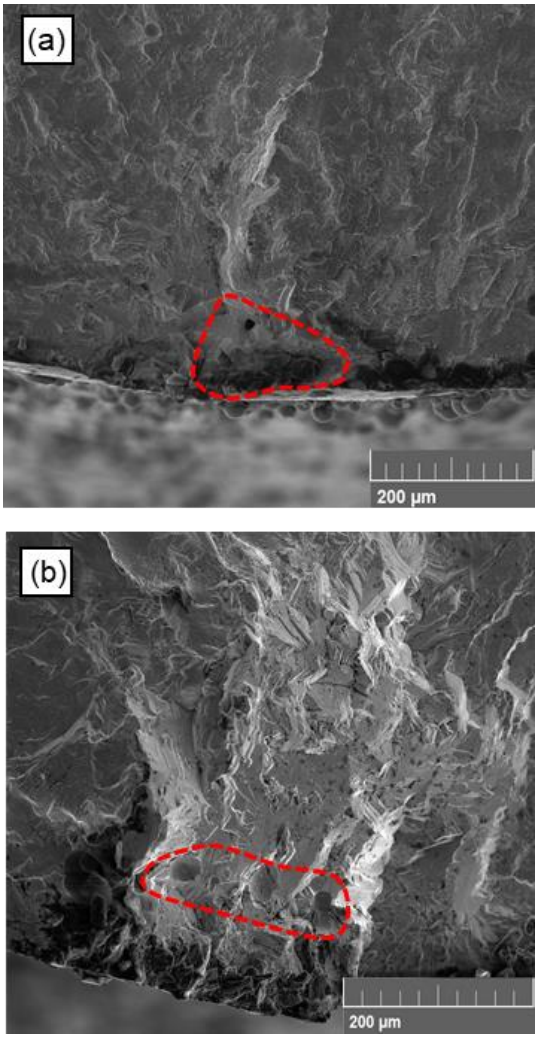

Figure 47. Magnified crack initiation sites from two as-built V specimens tested at σ_a = 200 MPa. The red dashed-line enclosed areas represent the failure initiating defect.

Using ImageJ software, the effective area $\sqrt{area}$ of the crack initiating defect was determined. For the specimen in Figure 45(a) the effective defect area is $\sqrt{area} = 107\ \mu m$ and $\sqrt{area} = 74\ \mu m$, for the specimen shown in Figure 47(b).

The defect of the specimen in Figure 47(a) is considered to be in touch with the surface, while the defect in Figure 47(b) is considered to be sub-surface. The Murakami [27]model requires knowledge of the material Vicker's Hardness, H_v. The LB-BF material's H_v value was not yet experimentally determined, so the known wrought Inconel 718 H_v value of 255 was chosen. The

results of the Murakami [27] fatigue limit estimation is presented in Table 5. Additionally, the Basquin equation estimated fatigue strength at 2 x 10^9 reversals is shown.

Table 5. Fatigue limit predictions at 2 x 10^9 reversals based on Murakami and Basquin methods

	Figure 44(a)	*Figure 44(b)*
$\sqrt{area}$ of defect (μm)	107	74
C value (for model)	1.41	1.56
Predicted σ_w (MPa)	243	285
Basquin predicted σ_w (MPa)	141	141

Based on the values shown in Table 5, it is clear that the Murakami [27] model is not a suitable approach for fatigue limit estimation. Rather, the Basquin curve-fit provides a much more realistic design parameter.

6. Conclusions and future work

In this thesis, a comprehensive study of the fatigue behavior of LB-PBF Inconel 718 was performed. The effects of surface quality and layer orientation on the fatigue resistance in HCF and VHCF regimes were investigated. LB-PBF specimens were fabricated and subjected to post-process heat treatment identical to that of the as-received wrought material. The effect of layer orientation on the fatigue resistance of the LB-PBF IN718 was investigated by fabricating specimens with layers oriented vertically and diagonally to the build platform. The effect of surface quality was subsequently investigated by comparing test results of post-process machined and polished specimens to as-built specimens. From the experimental results obtained in this thesis, the following conclusions were made:

The LB-PBF material used in this study, despite post process heat treatment, resulted in a grain structure that is unlike that of traditional wrought Inconel 718 variety. The matrix is comprised of columnar austenite grains exhibiting elongation in the direction perpendicular to the build plate. Both the LB-PBF and wrought materials contain strengthening precipitates; however, in the wrought material, these precipitates are along the grain boundary. In the LB-PBF material, Nb micro segregation (presumed to be γ" precipitates) forms a dendritic sub-granular structure. The influence of microstructure on fatigue resistance of the machined LB-PBF condition should be further studied, as the results suggest mechanical superiority of this build condition as compared to the wrought Inconel 718 used in this study.

As compared to the numerous literature reports (detailed in the literature review section of this thesis), the specimens used in this study have an overall low number of process-induced defects present within the LB-PBF material. This is because as-built (i.e., non-machined surface condition) specimens experienced high concentrations of LoF voids and un-melted powder particles at a depth of 100 μm below the part surface. The post-process machining used in this study removed most of these defects from the specimens.

The LB-PBF specimen fracture surfaces presented in this study did not resemble the appearance of fracture surfaces seen in previously published works by Yang et al. [31] and Gunther et al. [35]. Post-processed machined LB-PBF specimens showed no evidence of internal LoF defects, therefore the fatigue failure mode was dictated by the weakest link in the microstructure, rather than the largest defect. For all machined LB-PBF specimens in this study, the dominant HCF failure mode appears to be surface crack initiation in the absence of defects. Process-induced defects such as large pores within the material are only known to cause sub-surface crack initiation in machined LB-PBF specimens tested at low σ_a. No evidence of surface crack initiation was

observed for machined LB-PBF samples with fatigue lives exceeding 2 x 10^7 reversals. Samples tested in the as-built condition experienced significantly shorter fatigue lives as compared to their machined counterparts. This result is attributed to the high presence of surface flaws, such as un-sintered power, stair-step surface contours, and micro-notches.

Based on the discussions presented, the Murakami model proved to be insufficient for this material data. The Murakami model for fatigue limit prediction is more effective for materials with large defects that initiate single fatigue cracks. The machined LB-PBF specimens used in this study did not contain single crack initiating defects, rather multiple cracks with crack initiation sites that were difficult to identify and distinguish from crack propagation regions. The Murakami model also did not provide realistic results for the specimens tested in the as-built V condition. The Basquin equation, however, did provide a result that would have more closely matched the actual fatigue limit at 2 x 10^9 reversals. This result cannot be proven, because the USF tester used in this experiment was limited to a minimum σ_a of 200 MPa.

The LB-PBF material tested in the machined V condition exhibited superior fatigue resistance to the wrought material in the σ_a range of 600 – 800 MPa. Ultimately, the S-N curves of the wrought and machined V LB-PBF specimens converged at σ_a = 500 MPa. However, based on the contrasting microstructures of the wrought and LB-PBF materials used in this study, it is difficult to explain the disparity in fatigue resistance for these two specimen batches. The microstructure of the wrought Inconel 718 specimens contains a consistent grain structure, however there is a large, randomized dispersion of metal carbide precipitates throughout the matrix. Metal carbides have been known to act as crack initiation sites in wrought Inconel 718 in the VHCF regime [34]. In the V oriented LB-PBF microstructure, grains are refined along the plane of crack propagation (~11.4 μm along radial plane of V LB-PBF specimen as compared to

19 μm equiaxed grains in wrought material), which can aid in resistance of trans-granular crack growth. Additionally, it is clear that the post-process heat treatment (recipe matching the AMS 5662 standard) did not fully dissolve the as-fabricated Nb-rich dendritic structures. The differing microstructures of the wrought and LB-PBF materials present a need for further characterization of the LB-PBF material properties, such as microhardness, yield point, ultimate tensile strength, and work hardening exponent.

7. References

[1] W.E. Frazier, '"Metal additive manufacturing: a review," *Journal of Materials Engineering and performance*, vol. 23, no. 6, pp. 1917-1928.

[2] N. Shamsaei and J. Simsiriwong, '"Fatigue behaviour of additively-manufactured metallic parts," *Procedia Structural Integrity*, vol. 7, pp. 3-10.

[3] N. Shamsaei, A. Yadollahi, L. Bian and S.M. Thompson, '"An overview of Direct Laser Deposition for additive manufacturing; Part II: Mechanical behavior, process parameter optimization and control," *Additive Manufacturing*, vol. 8, pp. 12-35.

[4] M. Seifi, M. Gorelik, J. Waller, N. Hrabe, N. Shamsaei, S. Daniewicz and J.J. Lewandowski, '"Progress towards metal additive manufacturing standardization to support qualification and certification," *JOM*, vol. 69, no. 3, pp. 439-455.

[5] A. Yadollahi and N. Shamsaei, '"Additive manufacturing of fatigue resistant materials: Challenges and opportunities," *International Journal of .Fatigue*, vol. 98, pp. 14-31.

[6] M. Seifi, A. Salem, D. Satko, J. Shaffer and J.J. Lewandowski, '"Defect distribution and microstructure heterogeneity effects on fracture resistance and fatigue behavior of EBM Ti–6Al–4V," *International Journal of Fatigue*, vol. 94, pp. 263-287.

[7] P. Frye and J. Simsiriwong, '"An Overview of Very High Cycle Fatigue Behavior of Additively Manufactured Ti-6Al-4V," *Journal of Management & Engineering Integration*, vol. 12, no. 1, pp. 25-34.

[8] A. Du Plessis, I. Yadroitsev, I. Yadroitsava and S.G. Le Roux, '"X-ray microcomputed tomography in additive manufacturing: a review of the current technology and applications," *3D Printing and Additive Manufacturing*, vol. 5, no. 3, pp. 227-247.

[9] E. Wycisk, A. Solbach, S. Siddique, D. Herzog, F. Walther and C. Emmelmann, "'Effects of defects in laser additive manufactured Ti-6Al-4V on fatigue properties," *Physics Procedia*, vol. 56, pp. 371-378.

[10] W. Tillmann, C. Schaak, J. Nellesen, M. Schaper, M.E. Aydinöz and K. Hoyer, "'Hot isostatic pressing of IN718 components manufactured by selective laser melting," *Additive Manufacturing*, vol. 13, pp. 93-102.

[11] Z. Chen, X. Wu, D. Tomus and C.H. Davies, "'Surface roughness of selective laser melted Ti-6Al-4V alloy components," *Additive Manufacturing*, vol. 21, pp. 91-103.

[12] B. Vayssette, N. Saintier, C. Brugger, M. Elmay and E. Pessard, "'Surface roughness of Ti-6Al-4V parts obtained by SLM and EBM: Effect on the High Cycle Fatigue life," *Procedia engineering*, vol. 213, pp. 89-97.

[13] J. Gockel, L. Sheridan, B. Koerper and B. Whip, "'The influence of additive manufacturing processing parameters on surface roughness and fatigue life," *International Journal of Fatigue*, vol. 124, pp. 380-388.

[14] H. Nayeb-Hashemi, "'Failure modes of specimens containing surface flaws under cyclic torsion," *Experimental Mechanics.*, vol. 27, no. 1, pp. 51-56.

[15] P. Edwards and M. Ramulu, "'Fatigue performance evaluation of selective laser melted Ti–6Al–4V," *Materials Science and Engineering: A*, vol. 598, pp. 327-337.

[16] K. Solberg, J. Torgersen and F. Berto, "'Fatigue Behaviour of Additively Manufactured Inconel 718 Produced by Selective Laser Melting." *Procedia Structural Integrity*, vol. 13, pp. 1762-1767.

[17] D. Gopikrishna, S.N. Jha and L.N. Dash, "'Influence of microstructure on fatigue properties of Alloy 718," *Superalloys 718, 625, 706 and Various Derivatives.*

[18] P. Frye, M. Muhammad, J. Simsiriwong and N. Shamsaei, "'Very high cycle fatigue behavior of laser beam-powder bed fused Inconel 718," *Conference proceedings of the 2019 Solid Freeform Fabrication Symposium*, Austin, TX

[19] Y. Yamashita, T. Murakami, R. Mihara, M. Okada and Y. Murakami, "'Defect analysis and fatigue design basis for Ni-based superalloy 718 manufactured by selective laser melting," *International Journal of Fatigue*, vol. 117, pp. 485-495.

[20] S. Holland, X. Wang, J. Chen, W. Cai, F. Yan and L. Li, "'Multiscale characterization of microstructures and mechanical properties of Inconel 718 fabricated by selective laser melting," *Journal of .Alloys and Compounds*, vol. 784, pp. 182-194.

[21] R.M. Nunes, D. Pereira, T. Clarke and T.K. Hirsch, "'Delta phase characterization in Inconel 718 alloys through X-ray diffraction," *Iron and Steel Institute of Japan International*, vol. 55, no. 11, pp. 2450-2454.

[22] L. Zhou, A. Mehta, B. McWilliams, K. Cho and Y. Sohn, "'Microstructure, precipitates and mechanical properties of powder bed fused inconel 718 before and after heat treatment," *Journal of Materials Science & Technology*, vol. 35, no. 6, pp. 1153-1164.

[23] C. Silva, M. Song, K. Leonard, M. Wang, G. Was and J. Busby, "'Characterization of alloy 718 subjected to different thermomechanical treatments," *Materials Science and Engineering: A*, vol. 691, pp. 195-202.

[24] D. Zhang, W. Niu, X. Cao and Z. Liu, "'Effect of standard heat treatment on the microstructure and mechanical properties of selective laser melting manufactured Inconel 718 superalloy," *Materials Science and Engineering: A*, vol. 644, pp. 32-40.

[25] W.M. Tucho, P. Cuvillier, A. Sjolyst-Kverneland and V. Hansen, "'Microstructure and hardness studies of Inconel 718 manufactured by selective laser melting before and after solution heat treatment," *Materials Science and Engineering: A*, vol. 689, pp. 220-232.

[26] R.I. Stephens, A. Fatemi, R.R. Stephens and H.O. Fuchs, (2000) "'Metal fatigue in engineering," New York: Wiley

[27] Y. Murakami, (2002) "Metal fatigue: effects of small defects and non-metallic inclusions," Amsterdam: Academic Press, an imprint of Elsevier

[28] N. Shamsaei and J. Simsiriwong, "'Fatigue behaviour of additively-manufactured metallic parts," *Procedia Structural Integrity*, vol. 7, pp. 3-10.

[29] C. Berger and B. Kaiser, "'Results of very high cycle fatigue tests on helical compression springs," *International Journal of Fatigue*, vol. 28, no. 11, pp. 1658-1663.

[30] S. Siddique, M. Imran, E. Wycisk, C. Emmelmann and F. Walther, "'Fatigue assessment of laser additive manufactured AlSi12 eutectic alloy in the very high cycle fatigue (VHCF) range up to 1E9 cycles," *Materials Today: Proceedings*, vol. 3, no. 9, pp. 2853-2860.

[31] K. Yang, Q. Huang, Q. Wang and Q. Chen, "'Competing crack initiation behaviors of a laser additively manufactured nickel-based superalloy in high and very high cycle fatigue regimes," *International Journal of Fatigue*, pp. 105580.

[32] G. Qian, Y. Li, D.S. Paolino, A. Tridello, F. Berto and Y. Hong, "'Very-high-cycle fatigue behavior of Ti-6Al-4V manufactured by selective laser melting: Effect of build orientation," *International Journal of Fatigue*, pp. 105628.

[33] E. Wycisk, S. Siddique, D. Herzog, F. Walther and C. Emmelmann, "'Fatigue performance of laser additive manufactured Ti-6Al-4V in very high cycle fatigue regime up to 109 cycles," *Frontiers in Materials*, vol. 2, pp. 72.

[34] D. Texier, J. Cormier, P. Villechaise, J. Stinville, C.J. Torbet, S. Pierret and T.M. Pollock, '"Crack initiation sensitivity of wrought direct aged alloy 718 in the very high cycle fatigue regime: the role of non-metallic inclusions," *Materials Science and Engineering: A*, vol. 678, pp. 122-136.

[35] J. Günther, D. Krewerth, T. Lippmann, S. Leuders, T. Tröster, A. Weidner, H. Biermann and T. Niendorf, '"Fatigue life of additively manufactured Ti-6Al-4V in the very high cycle fatigue regime," *International Journal of Fatigue*, vol. 94, pp. 236-245.

[36] M.W. Tofique, J. Bergström and C. Burman, '"Very high cycle fatigue crack initiation mechanisms in different engineering alloys," *Procedia Structural Integrity*, vol. 2, pp. 1181-1190.

[37] S. Leuders, M. Thöne, A. Riemer, T. Niendorf, T. Tröster, H.a. Richard and H.J. Maier, '"On the mechanical behaviour of titanium alloy TiAl6V4 manufactured by selective laser melting: Fatigue resistance and crack growth performance," *International Journal of Fatigue*, vol. 48, pp. 300-307.

[38] J. Günther, S. Leuders, P. Koppa, T. Tröster, S. Henkel, H. Biermann and T. Niendorf, '"On the effect of internal channels and surface roughness on the high-cycle fatigue performance of Ti-6Al-4V processed by SLM," *Materials and Design*, vol. 143, pp. 1-11.

[39] P.D. Nezhadfar, R. Shrestha, N. Phan and N. Shamsaei, '"Fatigue behavior of additively manufactured 17-4 PH stainless steel: Synergistic effects of surface roughness and heat treatment," *International Journal of Fatigue*, vol. 124, pp. 188-204.

[40] F. Cabanettes, A. Joubert, G. Chardon, V. Dumas, J. Rech, C. Grosjean and Z. Dimkovski, '"Topography of as built surfaces generated in metal additive manufacturing: a multi scale analysis from form to roughness," *Precision Engineering*, vol. 52, pp. 249-265.

[41] T. Persenot, A. Burr, G. Martin, J. Buffiere, R. Dendievel and E. Maire, "'Effect of build orientation on the fatigue properties of as-built Electron Beam Melted Ti-6Al-4V alloy," *International Journal of Fatigue*, vol. 118, pp. 65-76.

[42] R. Shrestha, J. Simsiriwong and N. Shamsaei, "'Fatigue behavior of additive manufactured 316L stainless steel parts: Effects of layer orientation and surface roughness," *Additive Manufacturing*, vol. 28, pp. 23-38.

[43] D.B. Witkin, D. Patel, T.V. Albright, G.E. Bean and T. McLouth, "'Influence of surface conditions and specimen orientation on high cycle fatigue properties of Inconel 718 prepared by laser powder bed fusion," *International Journal of Fatigue*, vol. 132, pp. 105392.

[44] Shimadzu Corp., "'USF-2000A Ultrasonic Gigacycle Fatigue Testing System," 2020.

[45] D.H. Smith, J. Bicknell, L. Jorgensen, B.M. Patterson, N.L. Cordes, I. Tsukrov and M. Knezevic, "'Microstructure and mechanical behavior of direct metal laser sintered Inconel alloy 718," *Materials Characterization*, vol. 113, pp. 1-9.

[46] S. Sun, Y. Koizumi, T. Saito, K. Yamanaka, Y. Li, Y. Cui and A. Chiba, "'Electron beam additive manufacturing of Inconel 718 alloy rods: Impact of build direction on microstructure and high-temperature tensile properties," *Additive Manufacturing*, vol. 23, pp. 457-470.

[47] C. Bathias and P.C. Paris, (2004) "'Gigacycle fatigue in mechanical practice,", CRC Press.

[48] J.W. Pegues, S. Shao, N. Shamsaei, N. Sanaei, A. Fatemi, D.H. Warner, P. Li and N. Phan, "'Fatigue of additive manufactured Ti-6Al-4V, Part I: The effects of powder feedstock, manufacturing, and post-process conditions on the resulting microstructure and defects," *International Journal of Fatigue*, vol. 132, pp. 105358.

[49] H. Masuo, Y. Tanaka, S. Morokoshi, H. Yagura, T. Uchida, Y. Yamamoto and Y. Murakami, '"Effects of defects, surface roughness and HIP on fatigue strength of Ti-6Al-4V manufactured by additive manufacturing," *Procedia Structural Integrity*, vol. 7, pp. 19-26.

[50] A. Fatemi, R. Molaei, J. Simsiriwong, N. Sanaei, J. Pegues, B. Torries, N. Phan and N. Shamsaei, '"Fatigue behaviour of additive manufactured materials: An overview of some recent experimental studies on Ti-6Al-4V considering various processing and loading direction effects," *Fatigue & Fracture of Engineering Materials & Structures*, vol. 42, no. 5, pp. 991-1009.

[51] R. Molaei, A. Fatemi, N. Sanaei, J. Pegues, N. Shamsaei, S. Shao, P. Li, D.H. Warner and N. Phan, '"Fatigue of additive manufactured Ti-6Al-4V, Part II: The relationship between microstructure, material cyclic properties, and component performance," *International Journal of Fatigue*, vol. 132, pp. 105363.